

---

Electronic Thesis and Dissertation Repository

---

5-30-2022 9:45 AM

## On the effects of additive manufacturing process parameters on the performance of Hastelloy-X: A neutron diffraction experiment and crystal plasticity finite element model

Ahmed Aburakhia, *The University of Western Ontario*

Supervisor: Abdolvand, Hamidreza, *The University of Western Ontario*

A thesis submitted in partial fulfillment of the requirements for the Master of Science degree in Mechanical and Materials Engineering

© Ahmed Aburakhia 2022

Follow this and additional works at: <https://ir.lib.uwo.ca/etd>



Part of the [Other Materials Science and Engineering Commons](#)

---

### Recommended Citation

Aburakhia, Ahmed, "On the effects of additive manufacturing process parameters on the performance of Hastelloy-X: A neutron diffraction experiment and crystal plasticity finite element model" (2022). *Electronic Thesis and Dissertation Repository*. 8589.  
<https://ir.lib.uwo.ca/etd/8589>

This Dissertation/Thesis is brought to you for free and open access by Scholarship@Western. It has been accepted for inclusion in Electronic Thesis and Dissertation Repository by an authorized administrator of Scholarship@Western. For more information, please contact [wlsadmin@uwo.ca](mailto:wlsadmin@uwo.ca).

## Abstract

Additive manufacturing (AM) is increasingly becoming one of the favourable manufacturing techniques in various industries, such as transportation and energy. The reason for the extensive use of AM lies in the ability to use a wide range of process parameters for manufacturing engineering parts with complex geometries that cannot be effectively manufactured using traditional methods such as casting or forging. Understanding the role of process parameters is crucial for developing predictive models, as well as for manufacturing engineering components with the desired properties.

This research aims to characterize the influence of AM process parameters on the deformation mechanisms of Hastelloy-X, a nickel superalloy used in gas turbine engines. In-situ neutron diffraction, electron backscatter diffraction (EBSD) and crystal plasticity finite element (CPFE) analysis are used for this purpose. The Hastelloy-X samples were printed using laser power bed fusion (LPBF) AM technique. Here, attention is given to the effects of laser power and scanning speed. First, a literature review is provided in Chapter 2, which is followed by Chapter 3 that contains a detailed description of sample preparation, experimental set-up, and data processing. The results are presented and discussed in Chapter 4. Lastly, conclusions and future works are presented in Chapter 5.

The experimental results show that the microstructure, texture, and the degree of anisotropy of the printed samples significantly change with changing AM parameters. By comparing the evolution of lattice strains predicted from CPFE to those from experiments, it is shown that  $\{111\} \langle 110 \rangle$  is the active deformation mechanism in all printed samples.

Keywords: Additive manufacturing, Laser power bed fusion, Neutron diffraction, EBSD, CPFE

## Summary for Lay Audience

A broader view of this research is to understand the deformation mechanism of additively manufactured metals. Metal components are built by depositing the raw material, which is usually in the form of powder, on a substrate and then melt this layer by using a heat source. This process is repeated layer by layer until the final part is completely built. Traditional manufacturing processes have limitations in producing parts with complex geometries or require extensive post-manufacturing processes. Such limitations are addressed in additive manufacturing by controlling, for example, the layer thickness and the depositing position. However, the mechanical properties of the final component are significantly affected by the implemented process parameters. Characterizing the influence of such parameters on the mechanical performance of the printed parts ideally means that the process can be optimized to produce a component with the best possible mechanical performance. However, such characterization is not trivial to conduct, hence, crystal plasticity numerical modeling is introduced here to conduct simulations and study the effects of the complex microstructure of the printed part. This study focuses on characterizing the influence of changing laser power and scanning speed in the laser powder bed fusion process on a nickel superalloy's texture and mechanical properties. The numerical and experimental results reveal that while the microstructure of samples changes, their deformation mechanisms stay the same.

## Statement of Co-Authorship

All Hastelloy-X samples were printed at the National Research Council of Canada by Dr. Molavi-Zarandi. The preparation of samples prior to the experiment was handled by me and Dr. Abdolvand. These preparations include sample design, machining, polishing, and characterization with SEM and EBSD. The in-situ neutron diffraction measurements were conducted at ENGIN-X of the ISIS Pulsed Neutron and Muon Source, UK, under the 2055007 experiment and with the help of Dr. Kelleher. All simulations, data processing, figure preparation, and data interpretations provided in Chapters 3 to 6 were done by me.

## Acknowledgments

I would like to thank my family, especially my parents for supporting me throughout my academic journey. They are always the fuel that pushes me forward, not only in my academic life but also in my life journey. While they weren't present physically in London Ontario during my Western's journey, they managed to make their warm support as accessible as possible which helped me to excel in my journey. I would like to thank my wife, my daughter, my sisters and my brothers for their continuous support and love.

I would like to thank Professor Hamidreza Abdolvand for giving me the chance to work with him and his group. With his guidance, patience, and mentorship that have exceeded my expectations, I was able to complete my degree requirements. He was very supportive in all of my academic journey and his passion for the field has driven me to achieve more during my degree. His knowledge about material science is one of the factors that kept me motivated throughout my journey.

I would like to thank Dr. Ali Bonakdar and Marjan Molavi-Zarandi, for providing valuable insights to understand the project. Also, I would like to thank Dr. Joe Kelleher for providing valuable insight into the neutron diffraction experiment.

I would like to extend my gratification to MSDL group members. They enlightened me during group meetings with their valuable feedback. They also provided a warm environment to join in one of the most difficult times in history with Covid-19 present. Especially, I would like to thank Karim, Alireza, and Omid for their support, knowledge, and company.

I would like to acknowledge the NSERC program for supporting and funding this project, ISIS for providing the beamtime, and Siemens Energy for providing the materials.

# Table of Contents

Abstract.....	ii
Summary for Lay Audience .....	iv
Statement of Co-Authorship.....	v
Acknowledgments.....	vi
Table of Contents.....	viii
List of Tables .....	x
List of Figures .....	xi
Glossary.....	xiii
1. Introduction .....	1
• Motivation.....	1
• The scope of this research .....	3
• Outline.....	3
2. Literature Review .....	5
• Additive Manufacturing .....	5
• Nickel Superalloys .....	10
• Experimental Studies .....	14
2..1. Neutron Diffraction.....	14
2..2. Electron Back Scatter Diffraction:.....	17
• Modeling.....	18
3. Experimental procedure and model set-up.....	24
• Experimental procedure .....	24
• Model Set-up.....	27
4. Results and Discussion .....	33
• Experimental and modeling results .....	33
4..1. The initial microstructure and crystallographic texture .....	33
4..2. The average stress-strain curves.....	40
4..3. Lattice strains .....	42
• Discussion.....	45
4..1. General Trends.....	45
4..2. The effect of process parameters .....	47
5. Conclusions and Future Work.....	49



- Conclusions ..... 49
- Contributions ..... 51
- Future Work ..... 53

References ..... 54

Figures' Permission ..... 65

- Figure. 2-2 The main process parameters for the laser power bed technique [9] ..... 65
- Figure. 2-3 a, b: Fracture surface of a sample manufactured using non-optimum process conditions, arrows point to unmelted powder particles; c, d fracture surface of the sample that was manufactured using optimum process conditions [24] ..... 66
- Figure. 2-5 (a) Schematic of ENGIN-X Neutron Diffractometer [47] ..... 67
- Figure. 2-6 Schematic representation of Voce hardening law.  $\theta_0$  and  $\theta_1$  are the voce hardening parameters. [70] ..... 68

Curriculum Vitae ..... 69

## List of Tables

Table. 3-1 The process parameters used in this study. ....	24
Table.3-2 Nominal chemical composition (in wt%) of Hastelloy-X gas-atomized powder used for LPBF [8]. .....	25
Table. 3-3 Single crystal properties for Hastelloy-X were used in the CPFEE model.....	32
Table. 4-1 A comparison between the number of diffracting IP of {111} and {200} planes in specimens 1 and 2. Lattice strains are for the BD. ....	45

## List of Figures

Figure. 2-1 Different categories of AM processes based on the raw material. Adapted from [20].	7
Figure. 2-2 The main process parameters for the laser power bed technique [9].	8
Figure. 2-3 a, b: Fracture surface of a sample manufactured using non-optimum process conditions, arrows point to unmelted powder particles; c, d fracture surface of the sample that was manufactured using optimum process conditions [24].	10
Figure. 2-4 Diffraction: $d$ is the space between the diffracting planes, $2\theta$ is the diffraction angle and it is measured in the experiment, and $q$ is the scattering vector. Adapted from [41].	15
Figure. 2-5 (a) Schematic of ENGIN-X Neutron Diffractometer [47], and (b) the experimental setup at ENGIN-X, ISIS	17
Figure. 2-6 Schematic representation of Voce hardening law. $\theta_0$ and $\theta_1$ are the voce hardening parameters. [70].	22
Figure. 3-1 One of the printed samples with the coordinate system used in this study.	25
Figure. 3-2 Finite element input models for polycrystalline Hastelloy-X with 5184 distinct orientations on the TD-BD plane, (a) specimen 1 and (b) specimen 2. Elements are color-coded with respect to the $\Phi_1$ of the measured Euler angles.	29
Figure. 4-1 The initial microstructure of (a) specimen 1, (b) specimen 2, (c) specimen 3, and (d) specimen 4 were measured on the TD-BD plane. The corresponding EBSD maps of the TD-BD plane and SD-BD planes are respectively shown in the second and third columns. Grains are color-coded using inverse pole figure BD with the corresponding legend shown in (a). Red circles in (a) and (e) show the location of pores.	35
Figure. 4-2 A comparison between the experimental EBSD maps of (a) specimen 1, (b) specimen 2, (c) specimen 3, and (d) specimen 4 as measured on the TD-BD plane and the corresponding EBSD maps of	

the imported texture on the same plane, shown in the second column. Grains are color-coded using

inverse pole figure BD with the corresponding legend shown in (a)..... 366

Figure. 4-3 Pole figures of the specimens for the TD-BD planes: (a) specimen 1, (b) specimen 2, (c)

specimen 3, and (d) specimen 4. Pole figures for the SD-BD planes: (e) specimen 1, (f) specimen 2, (g)

specimen 3, and h) specimen 4. .... 38

Figure. 4-4 Neutron diffraction peak profiles for (a) specimen 1, (b) specimen 2, (c) specimen 3, (d)

specimen 4. Red represents BD, black represents SD. .... 40

Figure. 4-5 A comparison between the measured and calculated stress-strain curves for (a) specimen 1,

(b) specimen 2, (c) specimen 3, and (d) specimen 4..... 41

Figure.4-6 A comparison between the measured and calculated lattice strains along the BD for (a)

specimen 1 (c) specimen 2 (e) specimen 3 (g) specimen 4, and along the SD for (b) specimen 1 (d)

specimen 2 (f) specimen 3 (h) specimen 4. YS line represents the yield strength of each specimen. .... 43

## Glossary

AM	Additive manufacturing
AMed	Additively manufactured
BD	Build direction
Comp	Compression
CP	Crystal plasticity
CPFE	Crystal plasticity finite element
CPFEM	Crystal plasticity finite element modeling
CRSS	Critical resolved shear stress
EBM	Electron beam melting
EBSD	Electron back scattered diffraction
EDM	Electrical discharge machining
EHLMD	Extreme high-speed laser metal deposition
FCC	Face- centered cubic
FE	Finite element
FEM	Finite element model
HCP	Hexagonal close-packed

IP	Integration point
LPBF	Laser power bed fusion
LPBF-AM	Laser power bed fusion additive manufacturing
RSS	Resolved shear stress
SC	Self-consistent
SD	Scanning direction
SE	Specific energy
SEM	Scanning electron microscope
SF	Schmid factor
SLM	Selective laser melting
TD	Transverse direction
TOF	Time of flight
UMAT	User material
$F$	Deformation gradient
$F^e$	Elastic part of deformation gradient
$F^p$	Plastic part of deformation gradient
$L$	Velocity gradient
$L^e$	Elastic part of velocity gradient

$L^p$	Plastic part of velocity gradient
$D$	Strain rate tensor
$D^e$	Elastic part of strain rate tensor
$D^p$	Plastic part of strain rate tensor
$\Omega$	Spin rate tensor
$\Omega^e$	Elastic part of spin rate tensor
$\Omega^p$	Plastic part of spin rate tensor
$m^\alpha$	Slip direction
$n^\alpha$	Normal to the slip plane
$S^\alpha$	Schmid tensor
$P^\alpha$	Symmetric part of the Schmid tensor
$W^\alpha$	Asymmetric part of the Schmid tensor
$\Psi$	Kirchoff stress tensor
$J$	Jacobian matrix
$\sigma$	Cauchy stress tensor
$\varepsilon$	Strain tensor
$\varepsilon^e$	Elastic strain tensor
$\varepsilon^p$	Plastic strain tensor

$\gamma^\alpha$	Shear strain on the slip/twin system $\alpha$
$\tau^\alpha$	Resolved shear stress on the slip/twin system $\alpha$
$g^\alpha$	Current strength of the slip/twin system $\alpha$
$g_0^\alpha$	Critical resolved shear stress of the slip/twin system $\alpha$
$g_0^\alpha + g_1^\alpha$	Final back-extrapolated CRSS of the slip/twin system $\alpha$
$\theta_0^\alpha$	Initial hardening rate of the slip/twin system $\alpha$
$\theta_1^\alpha$	Asymptotic hardening rate of the slip/twin system $\alpha$
$\Gamma$	Accumulated plastic shear
$q^{\alpha\beta}$	A parameter describing the interaction between slip/twin system $\alpha$ and $\beta$
$h^{\alpha\beta}$	A parameter describing the interaction between slip/twin system $\alpha$ and $\beta$ and is a function of the introduced hardening law



# Chapter 1

## 1. Introduction

- Motivation

Nickel-based superalloys have been widely used in corrosive environments that require superior mechanical properties and high strength, especially at elevated temperatures [1]–[5]. For example, nickel alloys are used to manufacture turbine blades where the tip of the blade is required to have the ultimate mechanical performance under significant temperature gradients. Most of the nickel-based superalloys are strengthened by the presence of a secondary phase that hinders dislocation motion [6], which requires higher stresses for dislocations to move. However, solid solution hardening is used to strengthen Hastelloy-X which is a Ni-Cr-Fe-Mo single-phase alloy. The absence of the secondary phase improves the resistance of the material to cracking, as the secondary phases are mainly made of hard carbides that are reported to facilitate crack growth [3], [7]. Due to having face-centered cubic (FCC) crystals with many possible slip planes and slip direction in their operative slip systems, nickel-based alloys generally possess relatively good ductility which facilitates traditional mechanical processing, such as forging or cold-working [8]. However, Hastelloy-X is known to have high work hardening which makes it difficult to machine. Hence some new techniques, such as AM, have emerged to manufacture Hastelloy-X components which do not require much machining [9], [10].

Additive manufacturing (AM) is an advanced technique that can be used to manufacture near-net-shape components from metals, composites, polymers, and ceramics [9], [11]. In AM techniques, components are printed by incrementally depositing the starting powder of the

material on a substrate and selectively melting the powder by an energy source according to a predefined path. The whole process is iterative where parts with complex geometries are built layer-by-layer to almost net-shape objects [9], [10]. During this process, however, metal alloys can develop a very strong texture, depending on the process parameters used. The mechanical properties of printed parts significantly depend on the evolution of microstructure and texture, which subsequently affect the performance of the engineering component.

Laser power bed fusion (LPBF) has been extensively used for additive manufacturing of metal alloys. In this method, the initial powder is applied to a substrate where a laser beam selectively melts the powder to a given shape. Depending on the process parameters, materials with different microstructures or textures can be produced. Here, the main parameters are laser power, scanning speed, layer thickness, hatch spacing, and scanning strategies [9], [12]–[15]. While LPBF can be used to manufacture engineering components with complex geometries, it introduces complex orientation distribution among the grains due to its complex thermal cycles during the build. The development of texture can affect the mechanical properties of engineering components by inducing significant anisotropy which can be controlled by tuning the LPBF process parameters. When the scanning speed of the laser is either too low or too high, the ultimate tensile strength of the resulting Hastelloy-X will decrease as well as its ductility. This is due to the higher concentration of void and porosity resulting from the lack of energy to fully melt the initial powder when the scanning speed is high [16]. Moreover, when the scanning speed is low, more energy is dissipated to the material which results in higher residual stresses. Furthermore, altering the scanning pattern can result in different solidification patterns, and hence different grain sizes will be produced. For example, it is

shown that with using a strip rotation scan, Hastelloy-X specimens with random texture and good mechanical properties can be manufactured [17]. While various aspects of LPBF technique are studied in the literature, there is a lack of data on how the deformation mechanisms of the printed parts can be changed with the process parameters- this is the focus of the current study.

- The scope of this research

The objectives of this research are to investigate the influence of LPBF process parameters on the deformation mechanisms of nickel superalloys at the meso and macroscales. This research specifically focuses on the effects of laser scanning speed and laser power on Hastelloy-X samples. In-situ neutron diffraction experiments are conducted to investigate the development of internal strains for both loading and transverse directions. Moreover, EBSD analysis is implemented to import the initial texture to a CPFEE model which is used to simulate plastic deformation in the samples, and compare the numerical results to those from the experiments. With the use of CPFEE and as-measured microstructures, the influence of laser power and scanning speed on the samples' textures, as well as lattice strains are investigated.

- Outline

Chapter 1 provides a general introduction and discusses the objectives of this research. In Chapter 2, a literature review is conducted on the effects of additive manufacturing processes on nickel superalloys and advanced experimental and modeling methods. Chapter 3 discusses the experimental procedure that was followed, starting from sample preparations to neutron diffraction experiments. This chapter is categorized into three sections, preparation before the experiments, experimental procedure, and data post-processing. Four Hastelloy-X specimens

have been used in this study, each with different LPBF process parameters. The results of the in-situ experiments on these four specimens are presented and discussed in Chapter 4. Finally, Chapter 5 provides the conclusions and future work.

## Chapter 2

### 2. Literature Review

This thesis focuses on characterizing the effects of AM process parameters on the mechanical performance of nickel superalloys by using diffraction techniques, e.g., neutron diffraction and EBSD, as well as CPFEE numerical modeling. Therefore, this review is comprised of three sections: the first section focuses on the manufacturing processes and their application to Hastelloy-X, the second section focuses on the experimental techniques, and the third section reviews the application of crystal plasticity in modeling materials behaviour.

- Additive Manufacturing

AM is an advanced technique, where its various methods can be used to manufacture near-net-shape components from metals, composites, polymers, and ceramics [9], [11]. While additive manufacturing techniques are broad, this study focuses on standalone AM techniques that are used to manufacture engineering components. AM was first commercialized in the industry in 1987 [18]. In powder-based AM techniques, engineering components are printed incrementally by introducing the starting powder on the building platform and selectively melting the powder by an energy source according to a predefined path controlled by a computer, based on the geometry of the component. The whole process is iterative where the object is built layer-by-layer. Controlling the thickness of the layer can result in almost net-shape objects [9], [10] and lead to a geometrical anisotropy that can be employed by AM to benefit a given application. Printed parts usually have finer grains due to inherent high cooling rates in the process, which results in higher mechanical strengths [19]. That is, finer grains introduce higher dislocation densities into the microstructure in the form of grain boundaries which introduce a higher

mechanical resistance to dislocations movement. AM processes are generally categorized into seven different groups by the International Organization for Standardization. These groups are stereolithography, material jetting, binder jetting, material extrusion, powder bed fusion, sheet lamination, and direct energy deposition. In stereolithography, a laser beam is used to draw the boundary of the build on a vat of liquid photopolymer resin. The geometry of the whole build is controlled by controlling the build platform movements. In material jetting, the raw material is deposited on the build platform in the form of droplets. Controlling the droplets' dimensions characterizes the build quality. While the accuracy of this process is considered high, the processing time is also considered high. In binder jetting, a powder is used as the raw material along with a binder. The raw material is rolled over the build plate and then the binder is applied selectively on the raw material as per the geometry of the final part. While this process is considered fast and easily customizable, it usually requires detailed post-processing to achieve the required build precision. In material extrusion, the raw material is drawn, heated, and deposited on the build platform through a nozzle that controls the deposition and hence the final build. This process is used mostly for cheap builds with polymers as the raw materials. In powder bed fusion, the raw material is used in the form of powder, and it is deposited on the build platform. Then a source of thermal energy is applied to melt the powder selectively according to the final geometry of the part. This process can be further subcategorized based on the source of thermal energy. If an electron beam is used, it is called electron beam melting. If a laser is used, it is called laser powder bed fusion (LPBF) or selective laser melting (SLM). In sheet lamination, the raw material is used in the form of layers and the final build is achieved by binding the layers using welding techniques or an adhesive. In the direct energy deposition,

the raw material, in the form of wire, is melted and deposited continuously on the build platform using a thermal energy source, either a laser beam or an electron beam. The raw materials used in AM processes can be solid as in sheet lamination, liquid as in the binder jetting, or powder as in the powder bed fusion [20]. A more general view of the mentioned processes is presented in figure 2.1.

One of the recent developments in AM is extreme high-speed laser metal deposition (EHLMD) in which a laser beam with a bigger diameter is used to melt the powder on the substrate. The concept of using a big diameter laser is to subject the laser energy on melting the powder by covering a much larger area of the powder on the substrate and therefore, very low energy will penetrate the substrate. As a result, fast laser scanning speed can be employed in this process, which significantly reduces the production time without affecting the material cohesiveness [21].

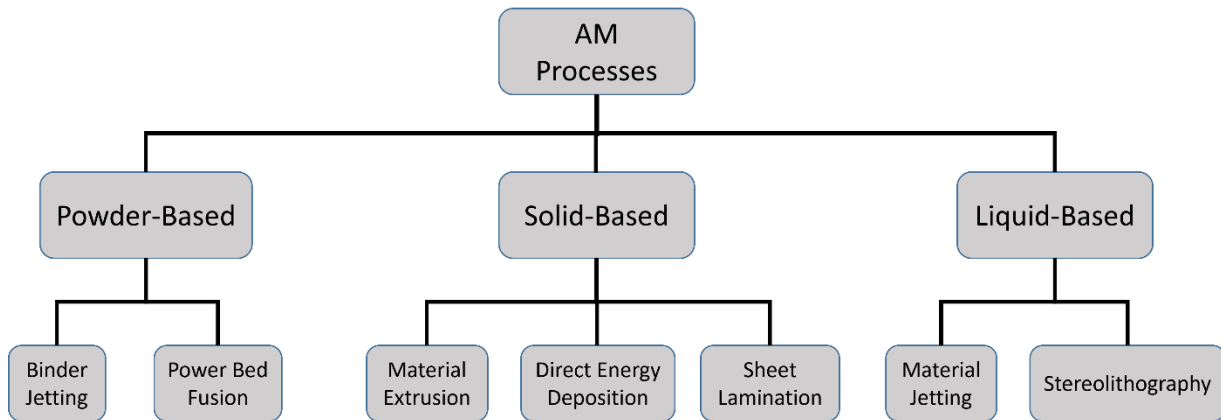


**Figure. 2-1 Different categories of AM processes based on the raw material. Adapted from [20].**

One of the AM processes that is mostly used for manufacturing metals and alloys is LPBF [12].

In LPBF, the initial powder is applied to a substrate and then a laser selectively melts the

powder based on the design of the final part. The parts manufactured by LPBF will have different final microstructures when different process parameters are used, even when the same initial powder is used. Here, different process parameters might lead to a different thermal history, such as a higher cooling rate. It was shown that better mechanical properties can be achieved in the parts printed using LPBF, compared to their wrought counterparts [22], [23]. The main process parameters in LPBF are laser power, scanning speed, layer thickness, hatch spacing, and scanning strategies as shown in figure 2-2 [9], [12]–[16]. Various metallic parts have been produced using LPBF, e.g., nickel-based superalloys [5], [13], [15]–[17], [22], [23], steel [12], [14] and aluminum alloys [12].

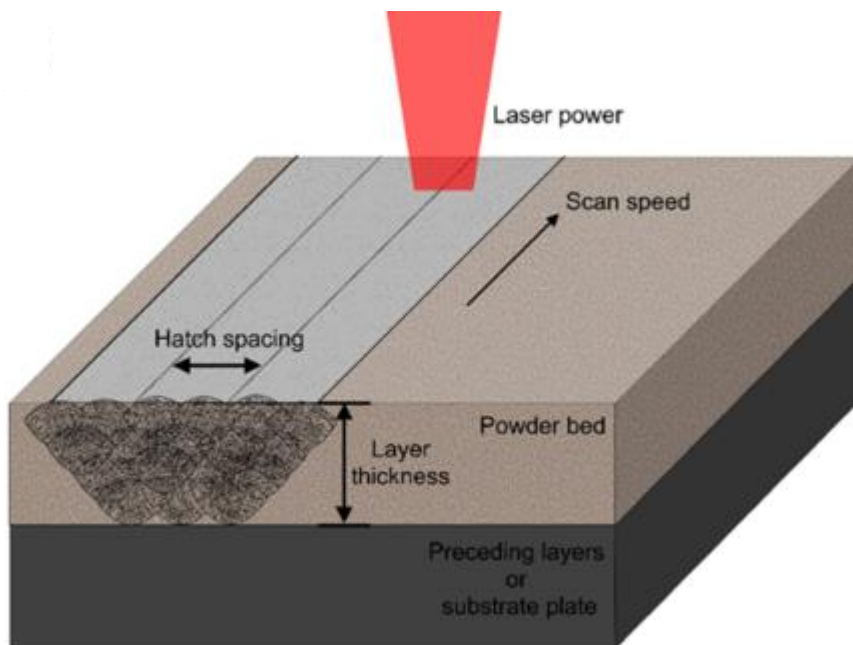


**Figure. 2-2 The main process parameters for the laser power bed technique [9].**

To examine the effects of LBPf process parameters on the microstructure and mechanical performance of the manufactured parts, several studies have been conducted. For example,



Esmailizadeh et al. showed that when the scanning speed of the laser is either too low or too high, the ultimate tensile strength of the resulting Hastelloy-X will decrease, as well as its ductility [16]. It was shown that when the laser speed is above a given value, partially melted particles will be present in the microstructure. For such cases, the finished parts tend to have a higher concentration of void and porosity. An example of a Hastelloy-X part built with partially melted particles is shown in figure 2.3. Some studies have focused on establishing a process window for a specific alloy that provides optimal mechanical performance. For instance, Wang et al. studied Hastelloy-X samples manufactured by LBPF, and proposed that for optimal mechanical performance, hatch spacing should be around 120  $\mu\text{m}$  [24]. In another study on Hastelloy-X [17], Keshavarzkermani et al. showed that changing the scanning pattern can result in different solidification patterns and hence different grain sizes will be produced. It was further shown that the Hastelloy-X samples with random textures and good mechanical properties can be produced if a strip rotation scan is used. In this process, the next deposited layer is rotated 67 degrees with respect to the previously melted layer. Furthermore, in another study conducted on stainless steel [14], Kamath et al. showed that for a given laser power, the density is negatively correlated with the scanning speed because of the inefficient powder melting. It was also reported that mechanical properties tend to be better in a specific build direction compared to others. Also, Liverani et al. [25], examined the effect of the scanning direction and reported that changing the build orientation from 90 to 45 degrees leads to an improvement in the strength and fatigue resistance of printed stainless steel. In a study conducted by Sanchez-Mata et al., the anisotropy of the manufactured LPBF-Hastelloy-X parts was investigated, and it was found that the highest yield and ultimate tensile strength was

along the  $\langle 111 \rangle$  orientation [13]. Keshavarzkermani et al. additively manufactured Hastelloy-X parts had higher strength than the ones manufactured with traditional processes [17]. In addition, AM has been used to produce metallic parts with specific crystallographic textures. For instance, the effects of beam type and laser power on the resulted texture of Inconel 718 were studied by Wang et al. [26]. In this study, specimens were successfully printed using SLM with a very strong texture along the  $\langle 100 \rangle$  direction.

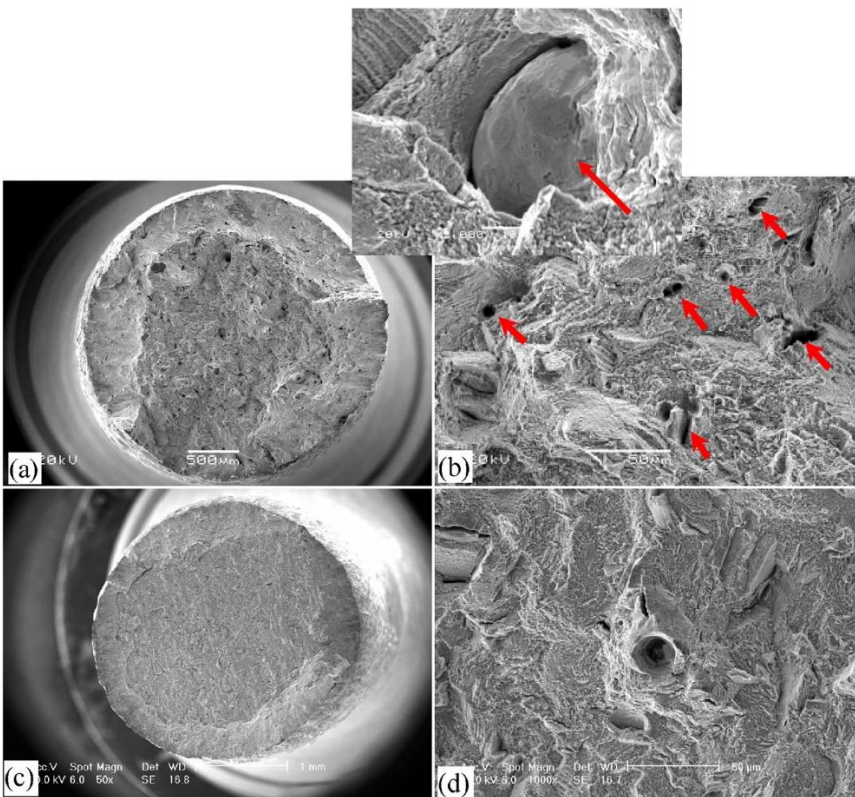


**Figure. 2-3 a, b: Fracture surface of a sample manufactured using non-optimum process conditions, arrows point to unmelted powder particles; c, d fracture surface of the sample that was manufactured using optimum process conditions [24]**

- Nickel Superalloys

Many critical industrial components, e.g., gas turbine, nuclear reactors, submarines, rocket engines, space vehicles, experimental aircraft, steam power plants, as well as other high-temperature applications rely heavily on nickel superalloys. Around 50% of the materials used in aerospace engines are nickel superalloys [27]. The operating environment in these industries is substantially harsh, which demands high-performance alloys for the elevated pressures and temperatures. Temperatures in the range of 600-950 °C and up to 37.5 MPa internal pressure are typical in these industries [28], [29].

While nickel superalloys are necessary for high-pressure high-temperature environments, there are several challenges in manufacturing them. Due to their high toughness and heat resistance, nickel superalloys are difficult to machine and require expensive cutting tools. Furthermore, nickel superalloys are subjected to a rapid work hardening, especially when a high-pressure environment exists [30]. These limitations challenge the industry standards in reducing the manufacturing cost, increasing the production rate, and producing high-integrity components [30]. This imposes certain limitations on the amount of post-processing that can be done on the traditionally manufactured nickel superalloys. Therefore, some studies have explored other techniques to increase the material removal rates (MRRs) in nickel superalloys [31]. Another challenge is that controlling the orientation of the traditionally manufactured nickel superalloys is always a difficult task, i.e., the default random texture resulting from the normal casting processes is not good enough for the intended application. To address this issue, directional solidification was introduced in the 1970s and it was possible to manufacture and use textured nickel superalloys in industrial applications [30]. With the advancement in the alloying and as more elements are added to nickel superalloys, directional casting became less efficient. Hence,

some other techniques have been developed to address the problem of low machinability of nickel superalloys. One of these techniques is called powder processing, where the initial material is an ingot that is melted inside a chamber with argon gas and then atomized and shaped into spheres. These spheres are grouped to resemble the geometry of the final part and pressed using hot pressing [32]. Although powder processing was initially introduced to manufacture ceramics, it was later adapted to metals, especially superalloys to address their machinability difficulties [30]. However, this process was not optimized for metals, hence, new techniques such as AM were needed to advance the functionality of nickel superalloys. AM techniques were initially limited to manufacturing prototypes, due to the limitations in their production volume as well as variations in the mechanical performance of the product. With the continuous advancement in AM techniques and the improvement of initial powder materials, AM became a more feasible option. One of the first productions of nickel superalloys was in 2014, when ARCAM (Möln dal, Sweden) produced Inconel 718 parts by using electron beam melting [18]. Since then, great advancements are achieved in AM that made it the optimal manufacturing method for nickel superalloys, especially for manufacturing near net shapes that require less machinability [33]. However, due to many factors either related to the initial raw material or AM process parameters, inconsistent results in the mechanical performance of the manufactured parts have been reported, which imposes challenges on relying on the engineering deployment of AMed components. Nevertheless, AM processes have been studied extensively to overcome such challenges. For example, the effects of changing the scanning strategy for reducing the possibility of cracking in CM247LC was studied by Carter et al. [34]. It was found that a simple back and forth scanning strategy is the best way to produce a

homogeneous columnar grain structure with {001} grains aligned towards the build direction. Such observation is critical as it would efficiently allow for printed parts with a preferred solidification direction resembling a more controlled directional technique. It has been shown that while AM can advance the performance of nickel superalloys, it comes with several challenges in terms of variations in melt pools, liquid-solid interface velocity, and thermal gradients [35]. A recent study suggests that a remelting process might be integrated with LPBF-AM, which would result in enhanced performance of nickel superalloys [36]. One of the main advantages of additive manufacturing is the level of control that it provides in building engineering components. For example, Wang et al., showed that, surface roughness of Hastelloy-X parts printed by LPBF can be greatly improved by reducing the layer thickness [24]. Further studies have also been conducted to characterize the effect of AM process parameters on the grain shapes of the printed samples. Graybill et al. [37] showed that grain shapes of the IN718 sample manufactured by Electron Beam Melting (EBM) are a function of the ratio of the thermal gradient over the cooling rate. When this ratio is high, i.e., high thermal gradient and low cooling rate, grains with columnar microstructure are nucleated. However, when the ratio is low, higher cooling rate and low thermal gradient, and equiaxed grains form [37]. AM is shown to be one of the suitable manufacturing processes for the future of nickel superalloys due to its ability to produce complex engineering geometries needed by industries. However, the effects of process parameters are not fully understood especially on the development of microstructure. This study is concerned with examining the influence of laser power and scanning speed on the resulting texture and the development of internal lattice strains of Hastelloy-X samples printed by LPBF-AM.

- Experimental Studies

Deformation in polycrystalline materials depends on various parameters, including elastic and plastic properties of single crystals, crystal structure, size, and shape, as well as orientation. At nanoscales, atoms are packed in a specific arrangement which can affect the material's properties. For example, in FCC metals, atoms are closely packed within the {111} planes which makes the {111} grains the hardest grains. This explains why FCC metals usually have their optimal mechanical properties along the <111> direction. As per definition, single crystals or grains are those grains that share the same orientation which defines their boundaries within the polycrystalline material. The orientation distribution of grains defines the material texture which is an important parameter in defining the mechanical performance of the material. Different diffraction techniques can be used to measure individual grain orientation or the average texture of the material, some of which are discussed in the following sections.

### 2..1. Neutron Diffraction

Neutron diffraction can be used to measure elastic strains or materials texture. In this section, this technique is explained, mostly based on references [38]–[45].

Similar to other diffraction techniques, e.g., X-ray or synchrotron X-ray, neutron diffraction is based on Bragg's Law, (Eq. 2-1) [46]:

$$n\lambda = 2d_{hkl}\sin\theta \tag{2-1}$$

where  $\theta$  is half of the diffraction angle,  $d$  is the interplanar spacing of the  $hkl$  planes,  $\lambda$  is wavelength, and  $n$  is the diffraction order. A schematic of diffraction is shown in figure 2-4.

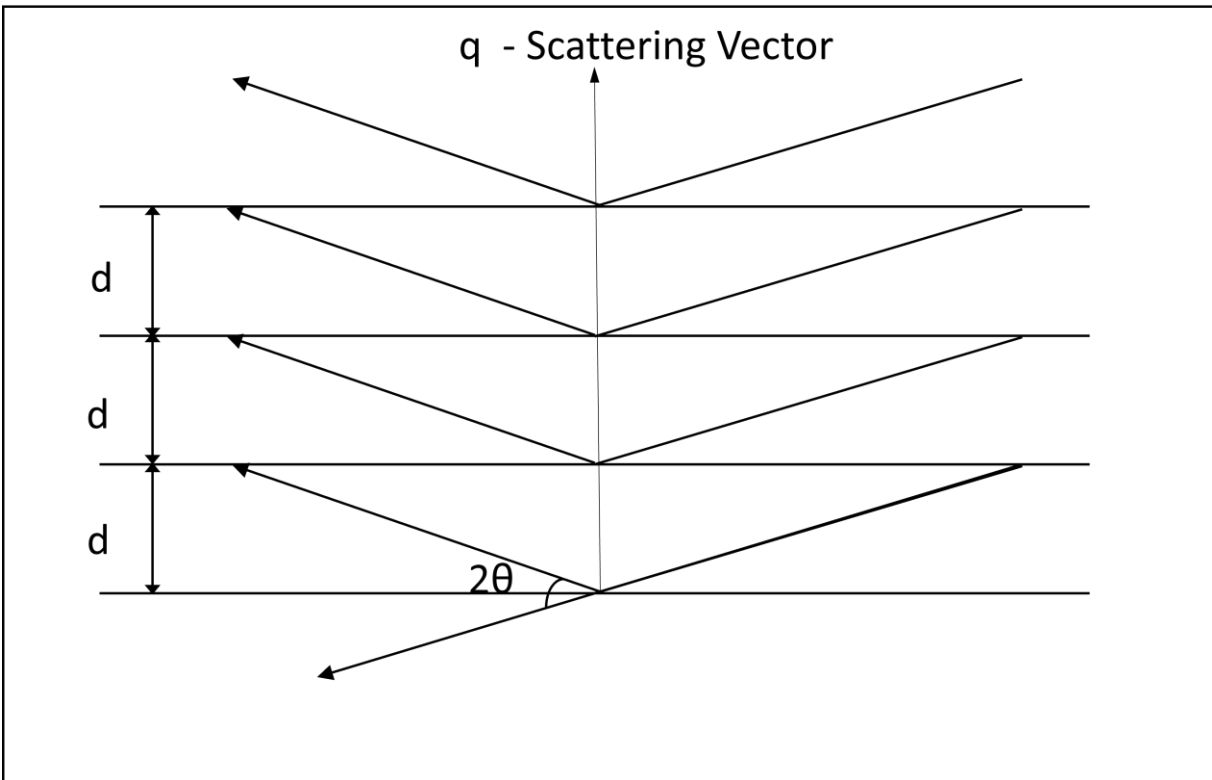


**Figure. 2-4 Diffraction:  $d$  is the space between the diffracting planes,  $2\theta$  is the diffraction angle and it is measured in the experiment, and  $q$  is the scattering vector. Adapted from [41].**

One distinct aspect of neutron diffraction is that neutrons can penetrate a few centimeters in most engineering materials, as opposed to few micrometers' penetration length in other diffraction techniques. However, for diffraction to happen, neutrons must have the wavelengths in the range of lattice spacing, i.e., thermal neutrons should be used. This relatively large penetration depth helps with averaging more grains which provide better statistics.

Lattice strain is the elastic strain that develops within grains with similar orientations that satisfy Bragg's condition for the given wavelength. While this strain is developing at the microscopic level, it directly affects material's behaviour at the macroscopic level because it

depends on how the load is shared between different sets of grains within the material. The lattice strain measurements in Chapters three and four of this thesis were carried out at the ENGIN-X beamline, ISIS, Rutherford Appleton Laboratory, UK.

A schematic of the test set up at ENGIN-X is shown in figure. 2-5. At ENGIN-X, a neutron whitebeam, which uses full bandwidth of neutron wavelengths, is collimated by slits and then passes through an adjustable aperture to define the gauge volume, which usually contains from hundreds to thousands of grains depending on the average size of the grains. The diffracted beam then passes through a radial collimator and reaches a bank of detectors. There are two detector banks perpendicular to the incident beam, each covering a range of angles [8]. At ENGIN-X, the Time Of Flight (TOF) concept is implemented, where a continuous spectrum of wavelength is used. In general, the pulsed beam is collimated to impinge on a specimen and is then diffracted towards a detector at a pre-selected diffraction angle. The time of neutron flight from the moderator to a detector is proportional to the neutron wavelength, which is proportional to the lattice spacing of the diffracting plane in the specimen [41]. By measuring the changes in the time of flight, one measures the changes in the plane spacing, i.e., lattice strain using the following equation, (Eq. 2-2):

$$\varepsilon_{hkl} = \frac{d_{hkl} - d_{hkl}^0}{d_{hkl}^0} = \frac{\lambda_{hkl} - \lambda_{hkl}^0}{\lambda_{hkl}^0} = \frac{t_{hkl} - t_{hkl}^0}{t_{hkl}^0} \quad (2-2)$$

Where d is the lattice spacing for the hkl planes,  $\lambda$  is the specific wavelength and t is the time of neutron flight. Here the index 0 is referring to the reference state which is usually the initial state before loading. Samples can be mounted at 45 degrees with respect to the incident beam to measure lattice strains parallel and perpendicular to the loading direction simultaneously.



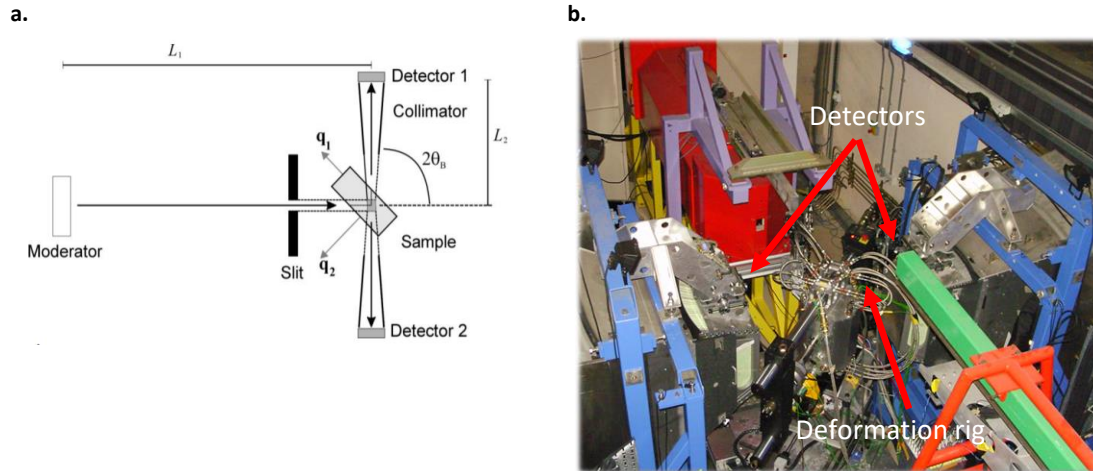


**Figure. 2-5 (a) Schematic of ENGIN-X Neutron Diffractometer [47], and (b) the experimental setup at ENGIN-X, ISIS**

## 2..2. Electron Back Scatter Diffraction:

Electron back Scatter diffraction (EBSD) is a diffraction-based technique that is used to measure the texture of polycrystalline material. The measured texture simply represents how grains are oriented with respect to the lab coordinate. EBSD has become a widely used technique in recent years due to the advancements in samples' preparations, availability of scanning electron microscopes, and the detailed information that an EBSD map provides. The first EBSD work was conducted by S. Nishikawa and S. Kikuchi in 1928, where a beam of 50 keV electrons was used on calcite at an angle of  $6^\circ$  [48]. EBSD is used in scanning electron microscopes (SEM), where electrons with specific energy and wavelength are shined onto the sample and interact with the surface atoms. The sample is tilted at an angle (typically in the range of  $\sim 60-70^\circ$ ) to reduce the energy loss of the electron beam. When an electron beam hits the surface of a sample, due to elastic interactions between the incident beam and planes of atoms, Kikuchi patterns are formed on the phosphor screen of the EBSD detector. Typically, more than one

Kikuchi band is formed, and measuring the angle between the bands along with the bands' width can lead to characterizing the grain orientations.

EBSD has been used extensively to characterize nickel superalloys. For example, Lin et al. conducted an EBSD analysis to examine the role of the  $\delta$  phase during a hot compressive deformation and found out that the presence  $\delta$  phase affected the nucleation and growth of the grains during dynamic recrystallization by inducing subgrains rotations [49]. In a more recent study on K648 superalloy manufactured by extreme high-speed laser metal deposition process (EHLMD), EBSD was used to examine the microstructure of the printed samples. It was shown that using this new advanced process, columnar grains are nucleated and grown in the build direction with fine equiaxed grains found between layers nucleated in the melt pool [21]. These studies show the power of EBSD in revealing key information about texture and microstructure. These characterizations are important in defining the materials' performance as grain morphology and orientation are the key elements in the anisotropy that affect mechanical performance.

- Modeling

The deformation mechanisms of polycrystalline materials are generally characterized by taking into account the properties and morphologies of single crystals and how they interact at different length scales. Crystal plasticity is a class of material constitutive equations that can be used for modeling deformation mechanisms of polycrystals. The principle of crystal plasticity is based on decomposing the deformation gradient into the elastic and plastic parts. The elastic part represents the elastic stretch of the crystal lattice and the plastic component represents the permanent deformation due to the motion of dislocations through the lattice- also known as

slip. To model texture evolution, the constitutive equations are used to update the orientation of each grain and its subsequent effects on the material's anisotropy. The concept of crystal plasticity was formed by the work of Taylor, Schmid, and their coworkers [50], [51] after the early qualitative observations of slip in aluminum. Various assumptions have been proposed to calculate the deformation or rotation of each grain; for example, Taylor proposed that each grain experiences the same strain as the applied one [52]. This observation is formulated in a theory called "full constraint theory" which calculates the upper bound stress. In this theory, each grain will be subjected to different stress conditions; as a result, force equilibrium equations will not be satisfied among grains. Another assumption was proposed by Sachs [20], where each grain is subjected to the same stress state as the one applied, resulting in the lower bound for stress. However, the Sachs model does not satisfy the compatibility equations. Other models were developed to address the interaction between grains, e.g., the self consistent (SC) modeling framework [53], [54] in which the interaction between adjacent grains is substituted by a simplified interaction of a grain with an average effective medium. In the SC framework, the true interaction between a grain and its surrounding neighbours is replaced by the interaction of the grain with a medium that represents all of the other grains. Another model that was used to model nickel superalloys is based on the Bodner Partom unified constitutive model where all plastic deformation mechanisms are modeled with a single kinetic equation that defines the plastic strain rate [55]. This model is based on a flow rule that relates the plastic strain rate to the deviatoric stress, a kinetic equation that characterizes the plastic strain rate to stress invariants by using a function that depends on temperature and internal state variables. While the model provides reasonably good results for nickel superalloys, its

application was limited to monotonic loading due to the simplifications carried out on the formulating equations. The most realistic representation of the interaction between grains can be achieved in the finite element framework where both equilibrium and compatibility equations can be solved, in the weak form, simultaneously. Another advancement in this area was achieved recently, where the exact solution to the equilibrium equations can be determined, by using a formulation that computes the local response of polycrystals based on a fast Fourier transform algorithm [56]–[58].

In the current research, the kinematic theory for mechanics of crystals is adopted to conduct the CPFE simulations. It was initially proposed by Hill [59], Rice [60], and Rice and Hill [61]; These equations were subsequently rewritten in the format that can be implemented in the finite element framework by Asaro and coworkers [62]–[65]. In the kinematic equations, it is proposed that the total deformation in a polycrystalline material can be decomposed into the elastic and plastic parts in which the former causes lattice stretching and rotation, and the latter causes shear in the crystal by the movement of dislocations on a specific plane, called the slip plane, and in a specific direction, called the slip direction.

Multiple slip systems (at most five systems) can contribute to the total plastic deformation of a polycrystalline material where shear in each slip system can be calculated by considering two different approaches. In the first approach, also called the rate-independent approach, Taylor assumed that between all of the possible combinations of slips systems, the set that minimizes plastic work rate contributes to deformation [52]. A solution to the Taylor assumption could

potentially be more than one set of systems, which causes the so-called “Taylor ambiguity”, which occurs when choosing different sets of slip systems can lead to different texture evolution. Alternatively, the energy assumption of Taylor was solved by Bishop and Hill [66] where the maximum work principle determines the deviatoric stress vector for a prescribed strain. In the second approach, a visco-plastic strain rate sensitivity [65], [67] is implemented, where shear can take place in all of the potentially active slip systems. This approach is called the rate-dependent scheme and is the one adopted in the current research. In this approach, the value of the shear is a function of the ratio of the resolved shear stress on each slip system and the current strength of the system [65], [67], [68]. The strength of the system can also evolve with the shear on each system. For instance, Pierce et al. [63] proposed a model in which the strength of each slip system correlates with the secant hyperbolic of the total shear on all of the systems. While the Peirce model is simple, Bauschinger effects cannot be captured in this model. Alternative models have been proposed when Bauschinger effects are of interest, e.g., Bassani and Wu [69]. In this research an extended Voce hardening rule [70] is used, where the strength of each slip system is proportional to the total accumulated shear on all of the systems (Eq. 2-3)

$$\tau^\alpha = \tau_0^\alpha + (\tau_1^\alpha + \theta_1^\alpha \Gamma) \left( 1 - \exp\left(-\frac{\theta_0^\alpha \Gamma}{\tau_1^\alpha}\right) \right) \quad (2-3)$$

where  $\tau$  is the strength of the system  $\alpha$ ,  $\tau_0$  is the critical resolved shear stress of the system  $\alpha$  and  $\Gamma$  is the accumulated plastic shear. The contribution of each parameter to the hardening law for each slip system is shown in figure 2-6. This is a phenomenological hardening law that has been used successfully in many prior models e.g., [70]–[72].

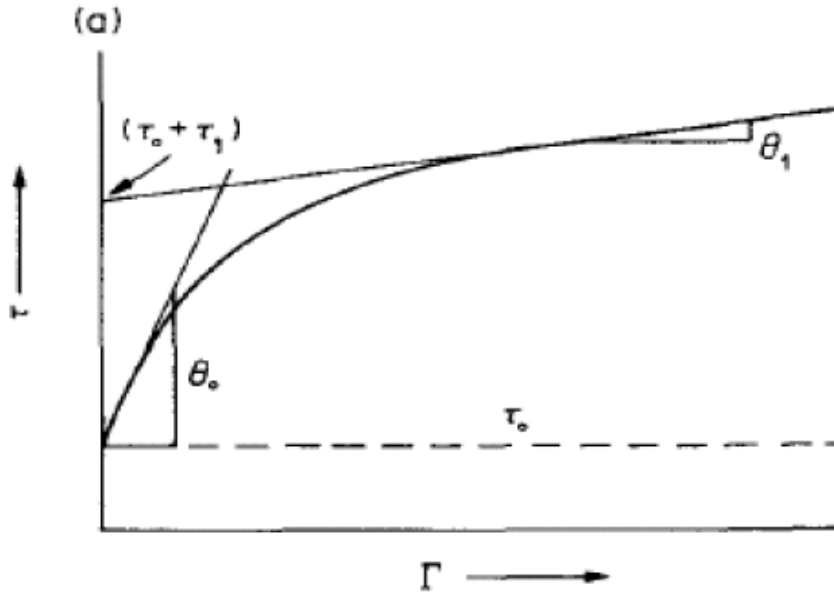


**Figure. 2-6 Schematic representation of Voce hardening law.  $\theta_0$  and  $\theta_1$  are the voce hardening parameters. [70].**

Hastelloy-X is a Ni-Cr-Fe-Mo single-phase alloy and has an FCC crystal structure. Generally, the strength and hardening of nickel superalloys depend on intermetallic compound precipitation in the FCC matrix [73] [3], [7]. Hastelloy-X, like many other nickel superalloys, does experience plastic anisotropy based on the applied loading condition. This anisotropy is further enhanced in 3D printed samples. For example, Coakley et al. examined the deformation mechanisms in polycrystalline nickel superalloys by examining the motion of diffraction peaks during a loading experiment, where each peak represents a family of grains sharing a common  $\{hkl\}$  diffraction plane and showed that the stress distribution between each grain is dependent on the orientation of the grains due to the elastic anisotropy of single crystals, while in the plastic region a redistribution occurs based on how easily grains deform [6]. The main deformation mechanism in nickel superalloys is the dislocation slip on their  $\{111\} \langle 110 \rangle$  octahedral slip

systems. However, some studies have reported the activation of other plastic mechanisms such as dynamic strain aging, twinning, and anomalous yielding with hot deformation [74]. For example, Abuzaid et al. [75] used digital image correlation and EBSD to investigate the role of the residual Burgers vector in slip transmission and plastic strain accumulation at the mesoscale and showed that the main deformation mechanism in Hastelloy-X manufactured by LPBF is the dislocation slip on  $\{111\}\langle 110\rangle$ . In this study, the main slip system considered active in modeling is  $\{111\}\langle 110\rangle$  with 12 variants. However, some studies were also conducted to test the activity of other reported mechanisms in nickel superalloys such as dislocation slip on  $\{111\}\langle 112\rangle$  [76], and deformation twinning that is orientation-dependent [13]. Another study conducted on a nickel superalloy showed that the primary deformation mechanism is the dislocation slip and it dictates the onset of plasticity as well as the initial yielding, but when the deformation continues, nano twins form [77].

## Chapter 3

### 3. Experimental procedure and model set-up

- Experimental procedure

Four Hastelloy-X samples were manufactured with an LPBF- EOS M290 machine using different process parameters as shown in Table 3-1. This research focuses on the influence of scanning speed ( $v$ ) and laser power ( $p$ ) on the final microstructure of the as-built parts. Therefore, all four samples were manufactured using the same parameters except for laser power and scanning speed. In addition, all samples were manufactured with the same powder, having a D90 of 46  $\mu\text{m}$ . The nominal chemical composition of the powder is provided in Table 3-2 [8].

**Table. 3-1 The process parameters used in this study.**

Sample#	Laser Power ( $p$ ), W	Scanning Speed ( $v$ ), mm/s	Hatch Spacing ( $d$ ), mm	SE, J/mm <sup>2</sup>
Sample1	150	1000	0.1	1.5
Sample2	150	600	0.1	2.5
Sample3	200	1000	0.1	2.0
Sample4	250	1000	0.1	2.5

A specific energy (SE) term is defined as  $SE = p/vd$ , where  $d$  refers to the hatch spacing. SE characterizes the amount of input energy per unit area of the build layer. The cross-section area of the LPBF as-built samples was  $1 \times 1 \text{ cm}^2$ , with 8 cm height (see figure 3-1). For the in-situ neutron diffraction experiments, compression specimens with the dimensions of 4 mm  $\times$  4 mm  $\times$  10 mm were cut from the as-built samples using wire electrical discharge machining (EDM).



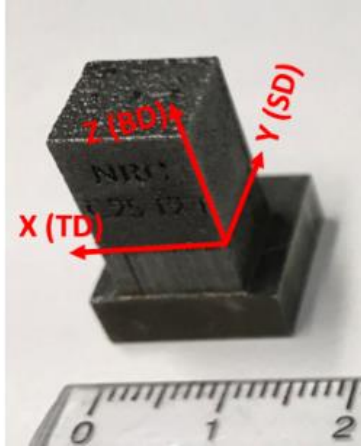


**Figure. 3-1** One of the printed samples with the coordinate system used in this study.

The dimensions of the compression specimens were chosen based on an FEM analysis to avoid buckling, which was confirmed during the experiment by monitoring macroscopic strain. Two other specimens from each sample were cut by EDM for analysis with EBSD, one cut on the X-Z plane and another one across the Y-Z plane as shown in figure 3-1. In this paper, Z refers to the build direction (BD), Y refers to the laser scanning direction (SD), and X is the transverse direction (TD) perpendicular to the other two. To prepare the specimen surfaces for EBSD analysis, all specimens' surfaces were first ground with silicon carbide paper from 320 to 1200 grit, polished with diamond suspensions of 6  $\mu\text{m}$ , 3  $\mu\text{m}$ , and 1  $\mu\text{m}$ , then finally finished with colloidal silica. The EBSD scans were subsequently performed with an acceleration voltage of 20 keV. Due to the presence of both small and big grains, a step size of 500 nm was used in all measurements to ensure all grains are indexed. An area of  $0.5 \times 0.5 \text{ mm}^2$  was scanned in each EBSD map.

**Table. 3-2** Nominal chemical composition (in wt%) of Hastelloy-X gas-atomized powder used for LPBF [8].

Ti	Al	Cu	Mn	Si	C	Co	W	Mo	Fe	Cr	Ni
< 0.15	< 0.5	< 0.5	< 1	< 1	< 0.1	$1.5 \pm 1$	$0.6 \pm 0.4$	$9 \pm 1$	$18.5 \pm 1.5$	$21.75 \pm 1.25$	balance

The in-situ uniaxial compression experiments were performed at the ENGIN-X neutron diffractometer, UK, using the time-of-flight (TOF) technique to acquire diffraction patterns. The TOF method is based on measuring the time it takes for neutrons created in a near-instantaneous pulse to travel from a moderator to the detector. This time is proportional to a wavelength, which is, in turn, proportional to lattice spacing for a given hkl diffracting plane through Bragg's Law, (Eq. 3-1) [46]

$$n\lambda = 2d_{hkl}\sin\theta \quad (3-1)$$

where  $\lambda$  is the neutron wavelength,  $d_{hkl}$  is the interplanar spacing of the hkl diffracting planes, and  $\theta$  is half of the diffraction angle. Under an externally applied load, the interplanar distance between atomic planes changes, and hence the internal elastic lattice strains can be calculated by measuring the change in the lattice spacing for a given hkl, (Eq. 3-2) [78]

$$\varepsilon_{hkl} = \frac{d_{hkl} - d_{hkl}^0}{d_{hkl}^0} \quad (3-2)$$

where  $d_{hkl}^0$  is the reference spacing for hkl planes before any load is applied and,  $d_{hkl}$  is the interplanar spacing when the material is subjected to the load.

- Model Set-up

The development of accurate constitutive models for simulating plastic deformation by slip and twinning in the finite element framework is an active research area [46], [51], [76], [79], [80]. In this study, however, CPFE modeling is used to investigate the variation of lattice strains in the printed specimens by changing the LPBF-AM process parameters. The details of the model used for simulating plastic deformation by slip can be found in [81], and only a brief description of the model is provided here. A UMAT subroutine is used that calculates the stress increments and updates a set of solution-dependent state variables based on the inputs provided by the ABAQUS FE solver, i.e., strain, rotation, time, and temperature increments. The total strain increment ( $\Delta\boldsymbol{\varepsilon}$ ) can be decomposed into the elastic ( $\Delta\boldsymbol{\varepsilon}^{el}$ ) and the plastic ( $\Delta\boldsymbol{\varepsilon}^{pl}$ ) parts.

Throughout this study, it is assumed that plastic strain is only affected by crystallographic slip because the specimens were only strained to 5%, where stresses are not anticipated to initiate any other plastic deformation modes. For calculating the plastic strain increment, the plastic part of the deformation rate ( $\mathbf{D}^{pl}$ ) is integrated over each time increment, i.e.

$$\dot{\boldsymbol{\varepsilon}}^{pl} = \mathbf{D}^{pl} = \sum_{\alpha=1}^{N^{spl}} \mathbf{P}^{\alpha} \dot{\gamma}^{\alpha} \quad (3-3)$$

$$\mathbf{P}^{\alpha} = sym(\mathbf{S}^{\alpha}) \text{ where } \mathbf{S}^{\alpha} = \vec{d}^{\alpha} \otimes \vec{n}^{\alpha} \quad (3-4)$$

where  $\mathbf{P}^{\alpha}$  is the symmetric part of the Schmid tensor ( $\mathbf{S}^{\alpha}$ ),  $\dot{\gamma}^{\alpha}$  is the shear rate on the slip system  $\alpha$ , and  $\vec{d}^{\alpha}$  and  $\vec{n}^{\alpha}$  are respectively the slip direction and the normal of the slip plane for the same slip system. The shear strain rate  $\dot{\gamma}^{\alpha}$  on each slip system is calculated using a rate-dependent equation [65]

$$\dot{\gamma}^{\alpha} = \dot{\gamma}_0 \left| \frac{\tau^{\alpha}}{g^{\alpha}} \right|^n \text{sign} \left( \frac{\tau^{\alpha}}{g^{\alpha}} \right) \quad (3-5)$$

where  $n$  controls the rate dependency,  $\dot{\gamma}_0$  is the reference shear rate of the slip system  $\alpha$ ,  $\tau^{\alpha}$  is the resolved shear stress acting on the slip plane and  $g^{\alpha}$  is the current critical resolved shear stress (CRSS) for the same slip system.

The resolved shear stress  $\tau^{\alpha}$  on each slip system is calculated using the symmetric part of the Schmid tensor  $\mathbf{P}^{\alpha}$  and the Kirchhoff stress  $\Psi$

$$\tau^{\alpha} = \mathbf{P}^{\alpha} : \Psi \quad (3-6)$$

The Jaumann rate of Kirchhoff stress ( $\check{\Psi}$ ) is calculated using

$$\check{\Psi} = \mathbb{C} : \mathbf{D}^e \text{ where } \check{\Psi} = \dot{\Psi} - \Omega^e \Psi + \Psi \Omega^e \quad (3-7)$$

where  $\mathbb{C}$  is the stiffness tensor, and  $\mathbf{D}^e$  and  $\Omega^e$  are the elastic parts of the deformation rate and spin tensors, respectively. They can be calculated using the symmetric and asymmetric parts of the elastic part of the velocity gradient. The strength of each slip system  $g^{\alpha}$  is assumed to follow an extended Voce hardening rule [81]

$$g^{\alpha} = g_0^{\alpha} + (g_1^{\alpha} + \theta_1^{\alpha} \Gamma) \left( 1 - \exp\left(-\frac{\theta_0^{\alpha} \Gamma}{g_1^{\alpha}}\right) \right) \quad (3-8)$$

where  $g^{\alpha}$  is the current CRSS,  $g_0^{\alpha}$  the initial CRSS,  $\Gamma$  accumulated shear on all slip systems,  $\theta_0^{\alpha}$  initial hardening rate, and  $g_1^{\alpha}$  and  $\theta_1^{\alpha}$  determine asymptotic characteristics of hardening.

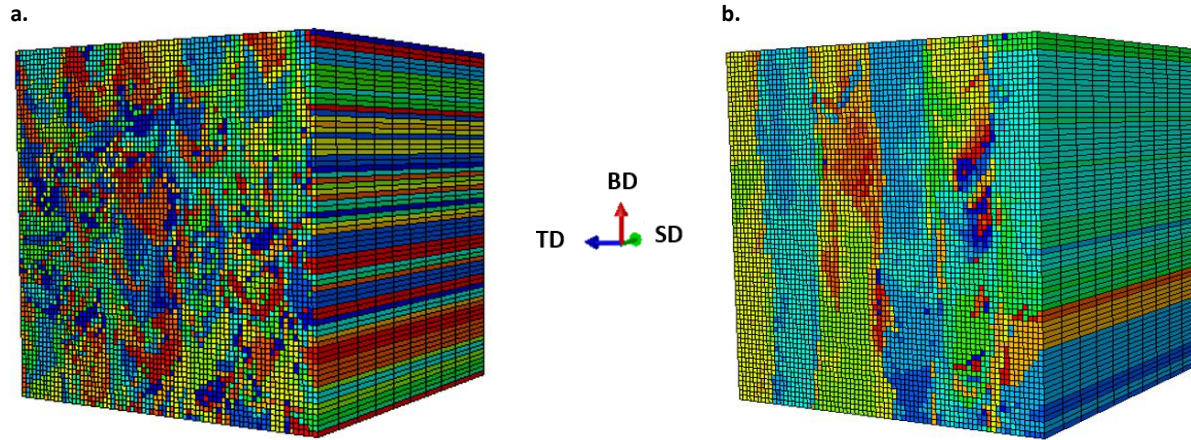


**Figure. 3-2 Finite element input models for polycrystalline Hastelloy-X with 5184 distinct orientations on the TD-BD plane, (a) specimen 1 and (b) specimen 2. Elements are color-coded with respect to the  $\Phi_1$  of the measured Euler angles.**

The FE input model is shown in figure. 3-2. To build the model in Abaqus, a cubic volume with a side length of 1 mm, located in the centre of the probed volume was meshed for CPFE modeling. First-order cubic elements (C3D8) were used for meshing the model cube. The crystallographic orientation of each modeled grain was measured using EBSD. The measured orientations from EBSD maps were assigned to elements, using the 2D coordinates of the measurement points and the coordinate of the element. No orientation averaging was done as EBSD results indicated significant orientation variations within each grain (see section 4.1.1), even before applying any load and plastic deformation. A total of 5184 (72 x 72) discrete orientations on the TD-BD plane (X-Z plane) were imported into the FE model and extend along the SD (Y-Axis) with 10 elements assigned to this direction, therefore, a total of 51840 elements were used in the modeled cube. The simple extrusion in the third direction is based on the results of the EBSD measurements on the BD-SD planes (Z-Y plane) where very few grains were measured on the BD-SD plane of the textured samples 2 and 4 (figures 4-1j and 4-1l). For

samples 1 and 3, a random texture is already assigned to the BD-TD plane of the model. The input models of the randomly-textured specimen 1 and highly-textured specimen 2 are respectively shown in figure. 3-2a and 3-2b. To check the validity of this procedure, the imported texture is compared to the experimental one for all four specimens and the results are shown in figure 4-2. It can be seen that most of the texture features of the experimental results are captured in the imported ones. A periodic boundary condition was applied to all input models to replicate the periodic microstructures of the printed specimens. All models were strained along the BD (Z axis) using the strain rate of  $5.5 \times 10^{-5} \text{ s}^{-1}$ . In addition, all models were strained to 5%, except for the one representing specimen 4, which buckled at 1.5% applied strain. As Hastelloy-X has single-phase FCC crystals [4], the main slip system considered active in modeling is  $\{111\} \langle 110 \rangle$  with 12 variants, although other systems are also tested and discussed in section 4.2.1

The elastic constants of Hastelloy-X single crystals were taken from Canistraro et al. and are provided in Table 3.3 [82]. The parameter  $n$  in (Eq. 3-5) controls materials rate dependency and many nickel-based superalloys are reported rate-independent, i.e.,  $n$  is equal to or greater than 50 [82]–[84]. Therefore, the value of  $n$  is set equal to 50, with  $\dot{\gamma}_0 = 0.003 \text{ sec}^{-1}$ . To the best of our knowledge, the parameters of Voce hardening law have not been reported for Hastelloy-X. Hence, in the modeling, the Voce hardening parameters  $g_0$ ,  $g_1$ ,  $\theta_0$  and  $\theta_1$  were taken as adjustable fitting parameters. The values of  $g_0$  and  $g_1$  were both initially taken as 175 MPa based on the values reported in [85]. The validity of the fitting parameters are examined by comparing CPFE results with the experimental ones. When the number of the fitting parameters is large, using one lattice strain curve is unlikely to pose sufficient constraints. That

is, various combinations of hardening parameters may lead to the same results. Fitting to a larger data set is obviously more difficult, but introduces more constraints leading to a better fit for the parameters. Therefore, an inverse approach was used in this study. This approach is based on adjusting the parameters in an iterative manner to simultaneously improve the fit to all the macroscopic flow curves and lattice strains. The data sets include 4 flow curves and 8 sets of lattice strains. The fitting parameters derived through such a process are more reliable than those derived through fitting to only one or two test and/or measurement directions. However, given the manual nature of this approach, they cannot be considered necessarily the best fit, and further, may not provide a unique solution. A summary of the single crystal parameters used in this study is presented in Table. 3-3.

Here, these parameters are tuned by using the values reported in the reference [85] as an initial guess and subsequently optimizing the agreement between the CPFEM and experimental results for the *macroscopic* stress-strain curves. A summary of the single crystal parameters used in this study is presented in Table. 3-3.

**Table. 3-3 Single Crystal properties for Hastelloy-X were used in the CPFEM model.**

Slip system	C <sub>11</sub> , GPa	C <sub>12</sub> , GPa	C <sub>44</sub> , GPa	g <sub>0</sub> , MPa	g <sub>1</sub> , MPa	$\dot{\gamma}_0, s^{-1}$	n	$\theta_0$ , MPa	$\theta_1$ , MPa
{111} <110>	227.7	155.5	118.7	230	120	0.003	50	550	120

To summarize, at the beginning of each time increment, the Abaqus FE solver sends the total strain ( $\Delta\varepsilon$ ) and time increments to the UMAT for calculating the increment of stress and the Jacobian matrix ( $J = \frac{\partial\Delta\sigma}{\partial\Delta\varepsilon}$ ) at each integration point (IP). Eq. 3-3 is used to calculate the increment of the plastic strain ( $\Delta\varepsilon^p$ ) considering the current state of the stress, and the magnitudes of the current shear strain increments from Eq. 3-5. Here, shear strain increments are calculated by multiplying the estimated shear strain rates ( $\dot{\gamma}^\alpha$ ) of Eq. 3-5 with the provided time increment. Once the plastic strain increment ( $\Delta\varepsilon^p$ ) is calculated, it is possible to calculate the increment of elastic strain ( $\Delta\varepsilon^e$ ) and the resulting stress increment from this equation,  $\Delta\varepsilon^e = \Delta\varepsilon - \Delta\varepsilon^p$ . The UMAT subroutine considers the effects of large deformation. Hence, a Newton-Raphson algorithm is used to iterate using the newly calculated values until the convergence at each time increment is achieved. This procedure is thoroughly discussed in Abdolvand et al. [46]. The updated  $\varepsilon^e$  and orientation of each IP is used to calculate the elastic lattice strain for a given  $hkl$  reflection in the directions of the measured scattering vectors  $q_1$  and  $q_2$ . The calculated values are subsequently compared with the measured ones from neutron diffraction to determine the deformation mechanisms of each specimen.



## Chapter 4

### 4. Results and Discussion

In this chapter, the experimental and numerical modeling results are presented. These are in the form of orientation maps, stress-strain curves, and lattice strain evolutions. The orientation maps acquired by the EBSD analysis are imported to the CPFEM model to calculate the average stress-strain curves as well as lattice strain developments and compare the numerical results to those measured in the experiment.

- Experimental and modeling results

#### 4.1. The initial microstructure and crystallographic texture

In this section, the measured initial microstructures and textures are analyzed. These measurements are used to prepare the CPFEM input files. The measured microstructures of all four specimens are shown in figure. 4-1. The first column represents the measured grain structures of the TD-BD plane using a scanning electron microscope, while the corresponding measured orientation maps for the TD-BD and SD-BD planes are respectively shown in the second and third columns. The results suggest that as the SE increases, the specimens become more textured. When the SE is  $1.5 \text{ J/ mm}^2$ , as in specimen 1 (figures. 4-1a, 4-1e, and 4-1i), the material has a random texture. However, when the SE is  $2.5 \text{ J/ mm}^2$ , as in specimen 2 (figures. 4-1b, 4-1f, and 4-1j) and specimen 4 (figures. 4-1d, 4-1h, and 4-1l), the resulting material is heavily textured with columnar grains, extended along the BD. For SE of  $2.0 \text{ J/ mm}^2$ , relatively textured material is produced as in specimen 3 (figures. 4-1c, 4-1g, and 4-1k). It has been shown that when a high scanning speed ( $1300 \text{ mm/s}$ ) is used, partially melted particles might exist in the microstructure [16]. Such phenomenon is associated with the increase in the laser speed,

which will reduce the provided thermal energy per unit time in the melt pool. Figures. 4-1a and 4-1e reveal similar effects in specimen 1, with low SE, where some pores are randomly distributed across the specimen. The observed pores are a result of the removal of these partially melted particles that happen during the polishing steps. The partially melted particles can also act as nucleation sites for new grains, which leads to the formation of randomly-textured specimens when a high laser scanning speed is used. It is worth noting that a low SE can be a result of high scanning speed, small hatch spacing, or low laser power.

When the SE is low, e.g., specimen 1, the laser power can barely melt the current layer. Therefore, grain nucleation is favorable on the new layer as opposed to grain growth from the previous layer. As SE increases, e.g., for specimens 2 and 4, there is enough energy to melt both the current layer and one or more previous layers. For such cases, grain growth is more favorable over grain nucleation, which leads to the development of a strong texture and the formation of columnar grains extended along the building direction. Such microstructure is observed in the EBSD maps of specimens 2 and 4, while a semi-columnar grain morphology is observed for specimen 3.

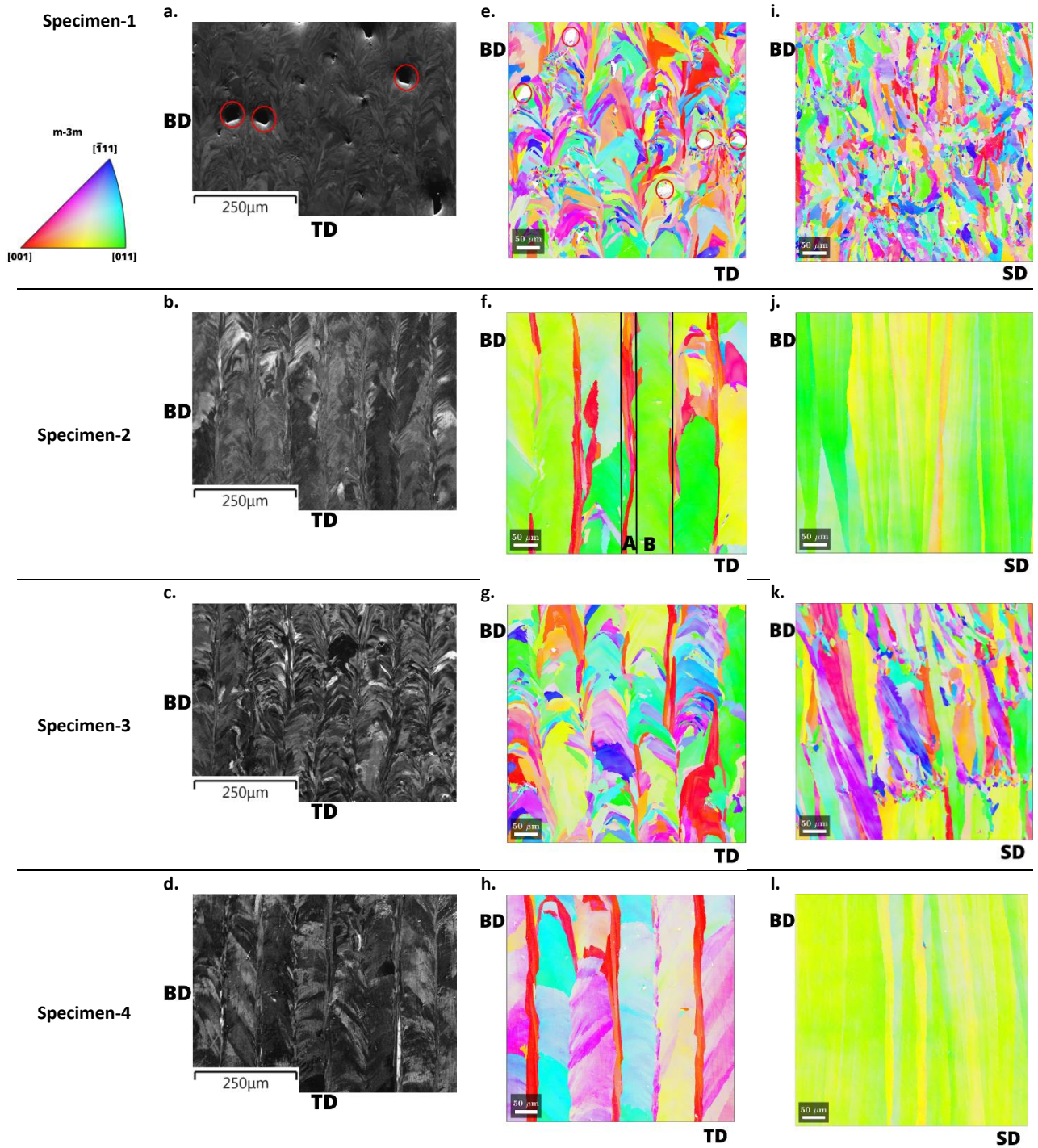


**Figure. 4-1** The initial microstructure of (a) specimen 1, (b) specimen 2, (c) specimen 3, and (d) specimen 4 were measured on the TD-BD plane. The corresponding EBSD maps of the TD-BD plane and SD-BD planes are respectively shown in the second and third columns. Grains are color-coded using inverse pole figure BD with the corresponding legend shown in (a). Red circles in (a) and (e) show the location of pores.

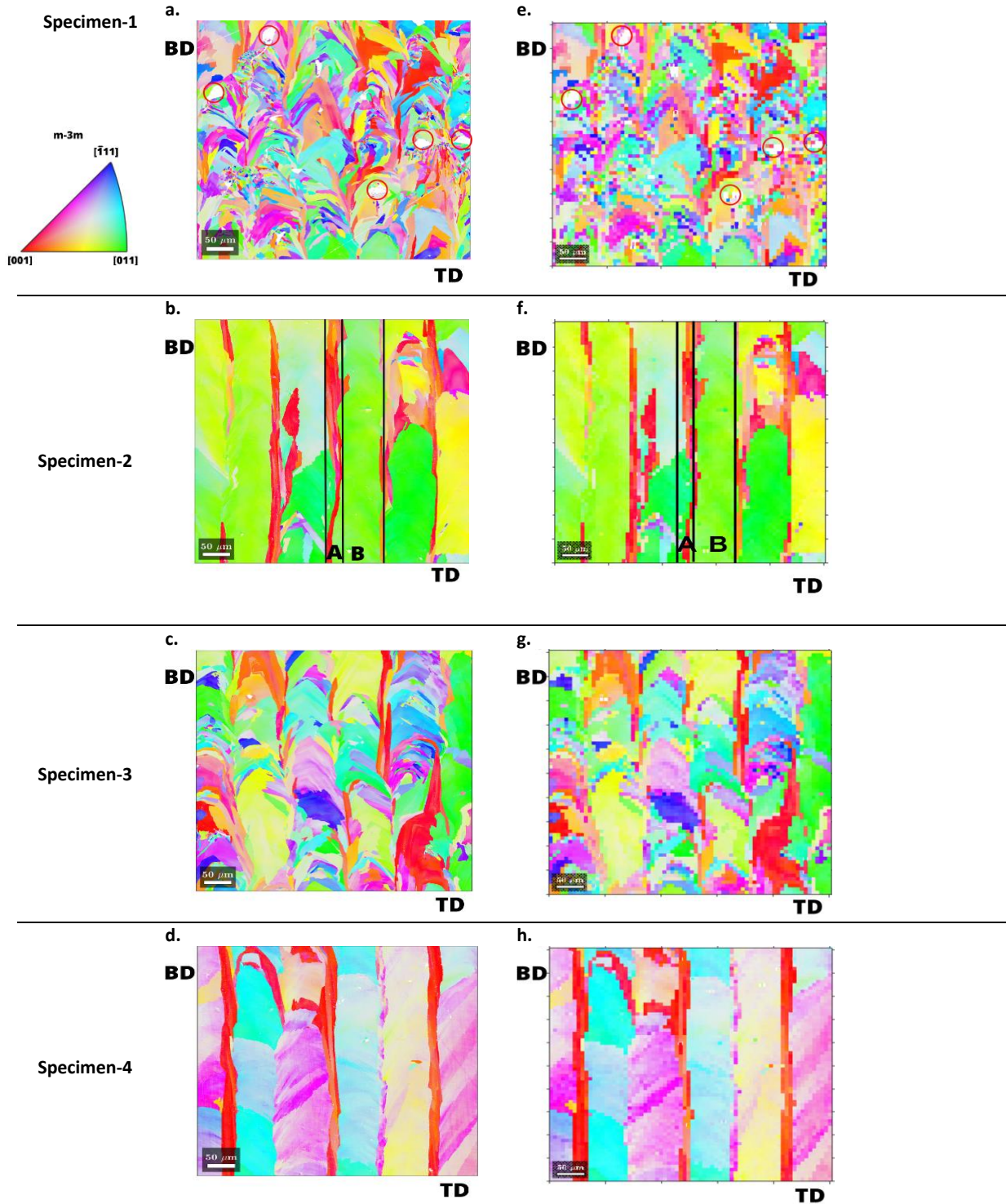
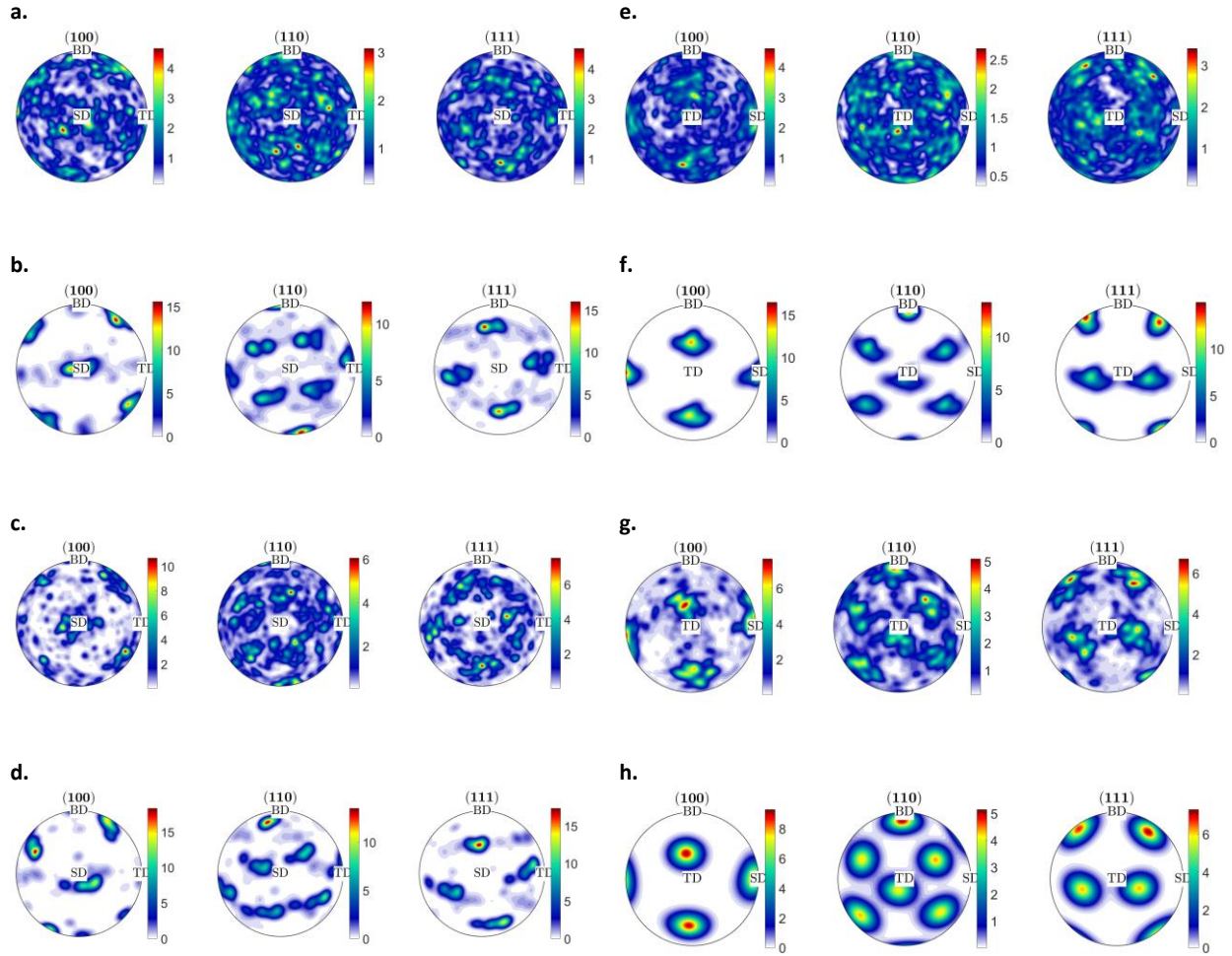


Figure. 4-2 A comparison between the experimental EBSD maps of (a) specimen 1, (b) specimen 2, (c) specimen 3, and (d) specimen 4 as measured on the TD-BD plane and the corresponding EBSD maps of the imported texture on the same plane, shown in the second column. Grains are color-coded using inverse pole figure BD with the corresponding legend shown in (a).

In figure. 4-1f, two distinct regions in specimen 2 are observed. The first layer, region A, was under the laser exposure and has a relatively uniform orientation. The second layer, region B, is a result of the merging of the two adjacent A-layers. B-layers are usually exposed to the laser energy more than just once and can be remelted in the LPBF process when the two adjacent A-layers are being melted, due to the use of higher SEs. Hence, they are more susceptible to orient towards the  $\langle 100 \rangle$ , which is the preferred growth crystallographic direction in FCC materials [17]. When the SE drops to  $2 \text{ J/mm}^2$ , as in specimen 3, these two distinctive regions still exist but are not continuous along the BD. Because of the reduction in the input energy, the thermal gradient in the melt pool is reduced, therefore, the capability of the laser to continuously melt the current and the previous layers is also reduced. Hence, shorter columnar grains are formed.





**Figure. 4-3 Pole figures of the specimens for the TD-BD planes: (a) specimen 1, (b) specimen 2, (c) specimen 3, and (d) specimen 4. Pole figures for the SD-BD planes: (e) specimen 1, (f) specimen 2, (g) specimen 3, and h) specimen 4.**

The calculated pole figures from the EBSD maps are shown in figure. 4-3. The first and second columns respectively represent the pole figures from TD-BD and SD-BD planes. It can be seen that while specimen 4 has a relatively stronger texture than specimen 2, especially along (100) and (111) planes of TD-BD measurement (see figures. 4-3b and 4-3d), specimen 2 has a stronger texture in the SD-BD plane (figure. 4-3f vs 4-3h).

Although the same SE was used for both specimens 2 and 4, a lower scanning speed was used for specimen 2 which provided more time for the laser to dissipate to the material during scanning, and hence more grains are oriented along the SD. By examining the orientation maps and pole figures along the TD-BD plane and SD-BD planes for the four specimens, some general trends can be observed. It is observed that (100) grains are oriented along the SD and their intensity increases as the SE increases. However, along the BD, (110) grains are more prevalent in all four specimens and their intensity also increases with SE. In addition, specimen 4 has a high population of (100) orientations along the BD, while it has the lowest population of (111) along the BD. Since (100) is the elastically softest orientation in FCC materials and (111) is the stiffest one, specimen 4 has the lowest overall modulus along the BD, which is also the loading direction.

The initial neutron diffraction profiles of the specimens are shown in figure. 4-4. In this figure, the red profile represents diffraction along the loading direction (BD) while the black profile represents the SD. Generally, the trends observed in the neutron diffraction profiles are consistent with those observed in pole figures. Specimen 1 has a random texture which is evident from the diffraction profile by the intensity of the 4 planes, i.e., {111}, {220}, {311}, and {200}, a trend that holds for both BD and SD directions. For the heavily textured specimens 2 and 4, very similar diffraction profiles are measured. For instance, the intensity of {200} planes along the SD is quite high, which is also consistent with the pole figures calculated from the EBSD maps. However, the intensity of the peaks in specimen 3 does not show as strong a variation as specimens 2 and 4 do, indicating that specimen 3 is a relatively textured material. It is worth noting that in all four specimens, {220} planes are oriented normal to the BD while the

{200} planes are oriented normal to the SD. In addition, in the textured specimens, the intensity of planes other than {200} and {220} is much lower. For example, in specimen 4, the {111} intensity is considerably lower than the intensity of the other planes.

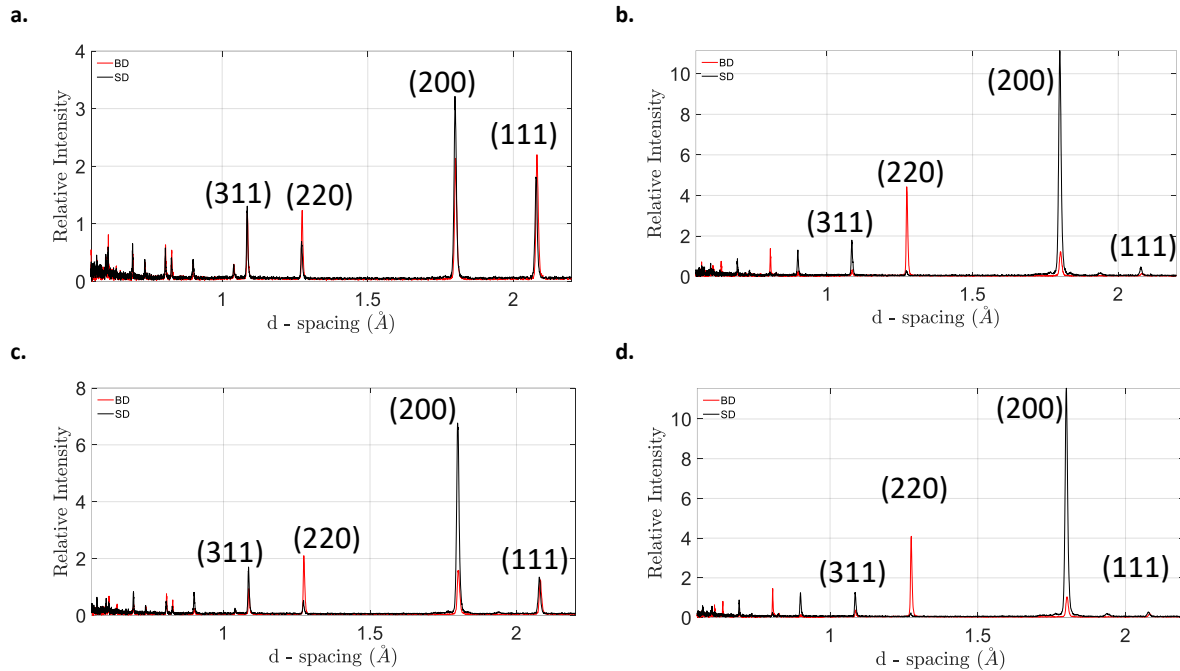


**Figure. 4-4 Neutron diffraction peak profiles for (a) specimen 1, (b) specimen 2, (c) specimen 3, (d) specimen 4. Red represents BD, black represents SD.**

#### 4..2. The average stress-strain curves

The measured and calculated stress-strain curves are shown in figure. 4-5. For CPFЕ results, the average stresses and strains at each time step are calculated by averaging all values from all IPs. Generally, good results were achieved using the single crystal parameters of Table 3-3. As illustrated in figure. 4-3, using different process parameters has produced different textures, which in turn has resulted in different elastic and plastic behaviours. Both experimental and numerical results show that the yield point for specimen 3 is slightly higher than specimens 2 and 4. In addition, both results show that the elastic modulus of specimens 1 and 3 is slightly lower than specimens 2 and 4. This is related to the texture and process parameters. As most of



the {001} poles (soft grains) are oriented towards the loading direction, and almost no {111} poles (hard grains) are oriented towards the loading direction in specimens 2 and 4, it is expected that a softer response is seen for these two specimens. In addition, the results shown for specimens 1 to 3 are up to 5% applied strain where no buckling was observed, however, an early buckling was observed in specimen 4, and hence data up to 1.5% applied strain is presented in this study. The early buckling is due to the heavy texture of this specimen and having the most {001} planes oriented towards the loading direction, with almost no {111} planes in the same. This is an evidence of strong elastic and plastic anisotropy resulting from the strong texture of specimen 4, which is the outcome of using different manufacturing process parameters.

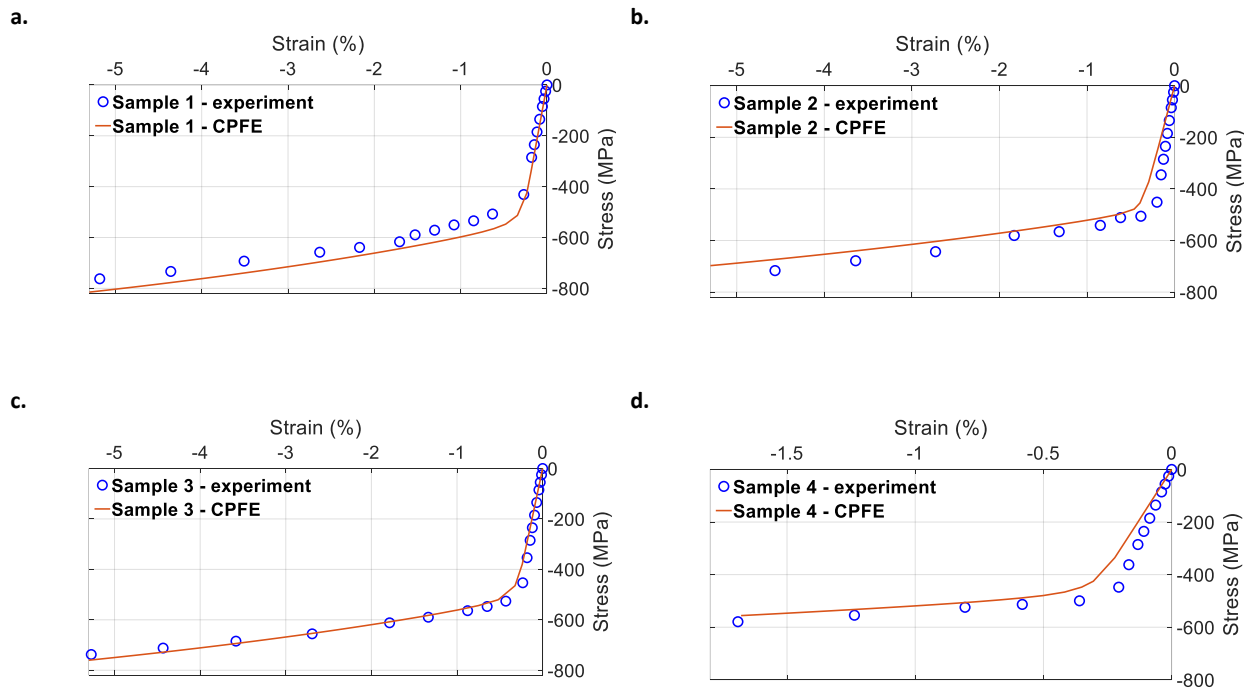


**Figure. 4-5** A comparison between the measured and calculated stress-strain curves for (a) specimen 1, (b) specimen 2, (c) specimen 3, and (d) specimen 4.

### 4.3. Lattice strains

Lattice strains were measured in-situ in both the loading and Poisson directions. For all four specimens, the loading direction is parallel to the specimen BD, while the Poisson direction is parallel to the SD. The measured and calculated lattice strains are shown and compared in figure. 4-6. Results presented in the left column are for the BD while those in the right column are for the SD. Lattice strains in the loading direction are negative because of the compressive load, but in the SD, the specimen expands from the Poisson effect and hence lattice strains are positive. All internal strains are plotted with respect to the macroscopic measured stresses. Generally, the experimental trends are well-captured by the CPFÉ model. For example, as expected for FCC materials, the {311} lattice strains hardly deviate from linearity in both model and experiment. The macroscopic yield point of each specimen is shown with the horizontal blue line where lattice strains start to deviate from linearity. In the simulation results, it is shown that in all specimens and for both measurement directions, the calculated lattice strains below the macroscopic yield points are in very good agreement with the experimental data, indicating that the elastic modulus used in CPFÉ simulations can accurately replicate the internal elastic strains.

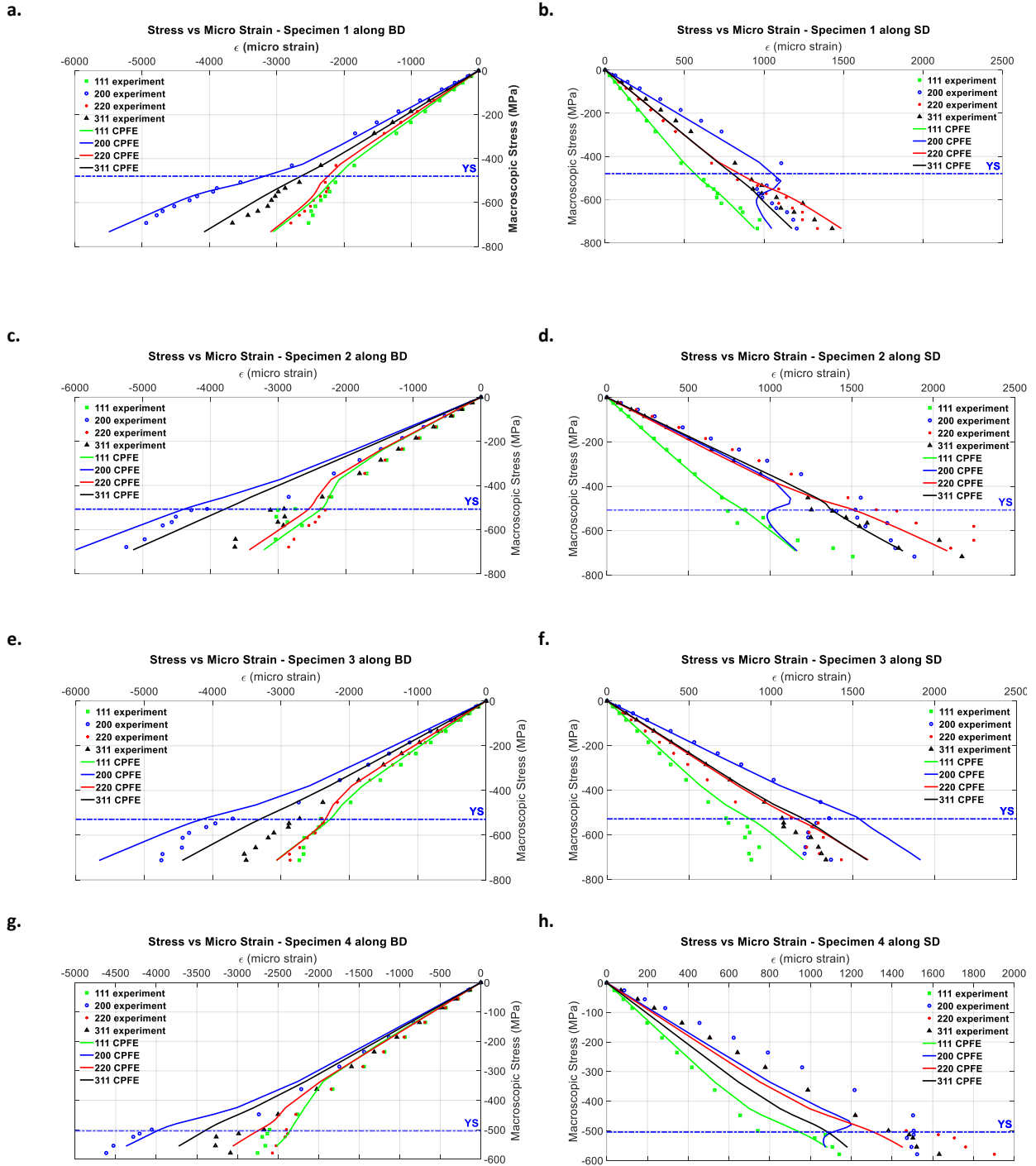


**Figure.4-6** A comparison between the measured and calculated lattice strains along the BD for (a) specimen 1 (c) specimen 2 (e) specimen 3 (g) specimen 4, and along the SD for (b) specimen 1 (d) specimen 2 (f) specimen 3 (h) specimen 4. YS line represents the yield strength of each specimen.

In the BD, two distinct inflections are observed in the {200} and {220} lattice strains of all specimens. Both modeling and experimental results show that {200} planes carry significant elastic strain. As shown in Table 4-1, CPFE results show that the number of diffracting IPs for {200} lattice strains decrease with loading while those of {220} lattice strains increase indicating that grains rotate towards {220}. This change in the number of diffracting IPs and the inflections observed in the lattice strains point to a load transfer among the grains, which was also reported for two other superalloys of nickel, Haynes 282 [74] and CM247LC [6]. Perhaps, a clearer load transfer is observed in the SD of specimen 1 (figure. 4-6b) where an abrupt significant inflection is observed in {200} lattice strains at around the macroscopic yield point. Interestingly, CPFE results replicate such an abrupt inflection in both {200} strains and the corresponding gradual change in {220} lattice strains. Results shown here indicate that the model was very successful in predicting the evolution of lattice strains for the complex microstructure of the alloy. In addition, lattice strains tend to evolve similarly along the BD and SD. For example, in both the BD and the SD, the stiffest grains are those with their {111} poles oriented along that direction. In addition, an abrupt change is observed in the {200} lattice strains measured along the SD, indicating a load transfer.

As shown in previous sections, the effects of AM process parameters are reflected in the texture development, which subsequently affects the evolution of lattice strains. Some of the measured lattice strains in the heavily textured specimens are generally noisy because of the low number of diffracting grains. For example, a comparison between the number of diffracting IPs between specimen 1 with random texture and the textured specimen 2 is provided in Table 4-1. Comparisons are made for the {111} and {200} lattice strains along the BD. It can be seen

that in specimen 1, more than 8325 IPs contribute to {111} strains while less than 480 IPs contribute to that of specimen 2. On the other hand, specimen 2 has more grains contributing to {200} strains compared to specimen 1.

**Table. 4-1 A comparison between the number of diffracting IP of {111} and {200} planes in specimens 1 and 2. Lattice strains are for the BD.**

Applied Stress - specimen 1 (MPa)	Number of Diffracting IP			Applied Stress- specimen 2 (MPa)	Number of Diffracting IP	
	{111}	{220}	{200}		{111}	{200}
-136.96	12432	21594	25488	-201.52	480	79676
-273.79	12431	21602	25488	-374.46	456	79568
-430.12	12070	21866	25376	-436.01	410	79703
-502.00	10999	22602	25140	-492.98	378	79708
-562.76	9975	23402	24762	-535.70	361	79633
-603.49	9470	24170	24470	-605.15	350	79439
-657.39	8873	25236	24063	-642.07	339	79247
-693.83	8525	25919	23833	-668.56	320	79045
-721.85	8325	26508	23664	-702.37	305	78796

- Discussion

#### 4..1. General Trends

LPBF-AM resembles welding, to a great extent, where a significant amount of heat is supplied to the powder material to melt and shape it to the required geometry. Such processes introduce significant thermal residual stresses in the material. The residual stresses are expected to increase with the supplied energy, i.e., as a function of SE. These residual stresses are not incorporated in the CPFE simulations, which could explain why the macroscopic stress-strain curves of figure. 4-5 for specimens 2 and 4 with SE = 2.5 J/ mm<sup>2</sup> are slightly underestimated. Such underestimation is at minimum for specimen 1 with the lowest SE = 1.5 J/ mm<sup>2</sup>, which correlates with the expected trends for residual stresses. In addition, one other

source of such underestimation could be associated with the development of strong texture in specimens 2 and 4, where columnar grains with minimum grain boundaries in the BD form. In comparison to specimens 2 and 4, more grain boundaries are observed in specimens 1 and 3. The presence of grain boundaries and misorientation induces localized stress fields near the grain boundaries as a result of the requirement to maintain compatibility. This subsequently contributes to the calculated macroscopic stress-strain curves and leads to an overestimation as observed for specimen 1 (figure. 4-5a). Nevertheless, most of the macroscopic and microscopic trends were captured in the numerical results using only one slip system,  $\{111\} \langle 110 \rangle$ , and with the use of a conventional crystal plasticity model. Hence, the microstructure, as well as the crystallographic texture, play a significant role in determining the underlying deformation mechanisms in additively manufactured Hastelloy-X specimens.

To examine the possible activity of other slip systems, CPFEM simulations were conducted using the same model setup, yet by activating other slip systems, e.g.,  $\{111\} \langle 112 \rangle$ . This slip system has been reported to play a role in the deformation of nickel-based superalloys [76]. However, the results did not show any improvements, suggesting that the primary slip system for Hastelloy-X is  $\{111\} \langle 110 \rangle$  and that this slip system is the most active system at the early stages of plasticity. In addition, the activation of  $\{111\} \langle 112 \rangle$  slip systems, reported in [76], is attributed to the presence of  $\gamma'$  as a secondary phase- this phase does not exist in the Hastelloy-X specimens used here, which can explain the absence of  $\{111\} \langle 112 \rangle$  activity in the current study.

## 4..2. The effect of process parameters

A 150 W laser power was used for both specimens 1 and 2, but the reduction in the scanning speed increases the energy input per unit time. The input energy along with the induced thermal gradients control the solidification process and, hence, the microstructure of the specimens. As the input energy increases, the chances that grains would rotate and a particular orientation forms towards the direction of the thermal gradient increase, resulting in a textured specimen as seen in specimen 2. It is suggested that the preferred growth direction along the BD in FCC metals during AM solidification is  $\langle 100 \rangle$  [17], [86], [87], however, the developed texture here in specimen 2 is along  $\langle 110 \rangle$ . This could be due to the use of insufficient input energy per unit time that prevents grains from fully orienting towards  $\langle 100 \rangle$ . Higher energy input would result in  $\langle 100 \rangle$  being oriented along the BD as Wang et al. [26] reported. Other process parameters, such as laser type or scanning strategy [87], might also influence the developed texture. Pauza et al. [88] reported that when Inconel 718 is printed with LPBF-AM using a  $SE = 3.2 \text{ J/mm}^2$ , the resulting microstructure has columnar grains with  $\langle 110 \rangle$  texture along the BD, consistent with the ones reported here for specimens 2 and 4 with  $SE = 2.5 \text{ J/mm}^2$ . Despite the strong microstructural differences between specimens 1 and 2, a similar trend is observed in the measured lattice strains in the BD for both specimens (figure. 4-6). Both specimens have nearly an identical behaviour along the BD except for the (111)-oriented grains carrying higher elastic strains in specimen 2. This could be related to the very low number of grains of specimen 2 oriented with (111) in the BD, which is also shown in the EBSD maps, pole figures, and Table. 4-1.

The contribution of laser power to the results can be analyzed by comparing specimens 1 and 3. Both specimens have the same scanning speed, but specimen 3 has a higher laser power. The increase in the laser power increases the SE, which subsequently induced a preferred orientation in specimen 3. Hence, both laser power and scanning speed need to be taken into consideration as both can affect the resulting microstructure.

Although both specimen 2 and specimen 4 have the same specific energy, specimen 2 has a slower scanning speed than specimen 4, while specimen 4 has a higher laser power. Despite the differences, the results show that both specimens have very similar macroscopic and microscopic behaviours. As presented in figure. 4-5, both specimens have a similar elastic modulus and yield strength, although specimen 2 possesses slightly higher yield stress due to having more {111} grains oriented towards (BD). In addition, in both specimens, the {200} lattice strain along the loading direction starts linearly with the same slope and remains linear up to 450 MPa, after which the {002} curve deviates towards higher negative values.

While only four specimens were used in the current study, a consistent trend was observed in the measured microstructures, textures, as well as lattice strains. With the use of CPFЕ and as-measured microstructures, it is shown that although their mechanical properties change in response to the degree of microstructural anisotropy, the deformation mechanism of the specimens remains consistent.

A conventional CPFЕ model was used here to study the development of internal strains in several specimens manufactured using the LPBF method. Some pores were observed in the EBSD and SEM images which were not accounted for in the CPFЕ simulations. Nonetheless, the



results of CPFEM simulations agree well with those measured with neutron diffraction. This indicates that the effects of pores are localized and are homogenized during both measurement and modeling. That is, to investigate the contribution of pores to microscopic and macroscopic behaviour of the alloy, more localized measurement techniques such as high-resolution EBSD (HR-EBSD) should be used. In addition, the contribution of pores will be more vivid when a tensile force is used. These are in the scope of our future studies.

## Chapter 5

### 5. Conclusions and Future Work

- Conclusions

The laser power bed fusion additive manufacturing technique was used to produce four specimens from Hastelloy-X. Different laser power and scanning speed were used to study their effects on the microscopic and macroscopic behaviours of the specimens. The initial microstructures and textures of the specimens on the build-transverse as well as on the build-scanning planes of the specimens were measured using EBSD. The as-measured EBSD maps were imported into a CPFEM model to study the effects of materials microstructures on the development of internal elastic strains. The numerical results were compared with those measured with in-situ neutron diffraction experiments. It is shown that:

- Specific energy, laser power, and scanning speed significantly affect the development of the material's texture and microstructure. Here, when SE is greater than  $2.0 \text{ J/mm}^2$ , a

columnar grain microstructure with  $\langle 110 \rangle$  texture along the build direction and  $\langle 100 \rangle$  along the scanning direction is observed. The development of strong textures at higher laser powers leads to the development of significant anisotropy in the mechanical properties of the printed specimens. The effects of such anisotropy are observed in both internal lattice strains and macroscopic stress-strain curves.

- The CPFÉ model was successful in replicating both the microscopic and macroscopic mechanical behaviour of the four specimens.
- For the range of the applied strain, it was shown that only  $\{111\}\langle 110 \rangle$  slip system was active in all specimens.
- The difference in the development of internal strains for the two highly textured specimens is at a minimum.
- The measured internal strains along the build direction for all specimens follow the same trend, yet some differences are observed in the location of yield points and deviation from linearity. Such differences are particularly vivid in the  $\{200\}$  lattice strains measured in the Poisson direction. CPFÉ simulations show that this is due to the differences in the microstructure and texture of the specimens.
- Lowering the SE to  $1.5 \text{ J/mm}^2$  produces specimens that are randomly textured with more equiaxed grains, in comparison to other specimens.
- The highest yield strength was observed in specimen 3 with an intermediate SE of  $2.0 \text{ J/mm}^2$ .

- Some pores were observed in specimen 1, which has the lowest SE. Also, two distinct regions were observed in the microstructure of specimens 2 and 4, with higher SE. The narrower regions in both specimens have {001} planes oriented towards the build direction.

- Contributions

This section provides a brief summary of the contributions made to simulate the additively manufactured nickel superalloy, Hastelloy-X, using CPFЕ. These contributions are:

- Two EBSD orientation maps were captured for each specimen on different planes, one on the BD-SD plane and another one on BD-TD, to characterize how the process affects the morphology of the grains.
- Although the texture and microstructure of the material change significantly with process parameters, CPFЕ modeling shows that the deformation mechanism of Hastelloy-X does not change, and {111}<110> is the dominant slip system.
- Internal strain development using neutron diffraction for both loading and transverse directions, which are important for model development, are presented in this study.
- This study shows how texture evolves during in-situ loading of Hastelloy-X and provides a recipe for how such effects should be studied in additively manufactured materials.
- This study uses more than 5000 as-measured orientations that are directly mapped to a FE model. Here we are providing a useful recipe for how to correctly conduct CPFЕ

modeling to understand complicated microstructures such as those developed in AM processes.

- It is shown that for compression tests, the CPFEM model works well for additively manufactured nickel superalloys.
- This study focuses on the effects of crystal elastic and plastic anisotropy on the macroscopic anisotropy of Hastelloy-X.

- Future Work

The next step in this research is to study deformation of AM samples under tensile tests and update the CPFEE model to incorporate the effects of pores. In this study, EBSD maps were measured on both BD-SD and BD-TD planes, and the orientations measured on the BD-TD were imported to the CPFEE model and extended along the SD. This is based on the observation that in the BD-SD plane we only measured 5-10 grains in 0.5 mm. Hence, columnar grains are a good approximation for the third direction for samples 2 and 4. This assumption basically means that the grains are modeled as perfectly columnar. However, orientation variations along the BD-SD should also be considered in modeling.

## References

- [1] Haynes International Inc., "HASTELLOY® X ALLOY A nickel-base alloy with an exceptional combination of oxidation resistance, fabricability and high-temperature strength. H-3009A," 1997.
- [2] Culling, John H. "Heat and corrosion resistant iron-nickel-chromium alloy." U.S. Patent 5,310,522, issued May 10, 1994.
- [3] Graybill, Benjamin, Ming Li, David Malawey, Chao Ma, Juan-Manuel Alvarado-Orozco, and Enrique Martinez-Franco. "Additive manufacturing of nickel-based superalloys." In International Manufacturing Science and Engineering Conference, vol. 51357, p. V001T01A015. American Society of Mechanical Engineers, 2018.
- [4] Zhao, J-C., M. Larsen, and V. Ravikumar. "Phase precipitation and time–temperature-transformation diagram of Hastelloy X." *Materials Science and Engineering: A* 293, no. 1-2 (2000): 112-119.
- [5] Shixiang, Shi, Eric H. Jordan, and Kevin P. Walker. "Self-consistent constitutive modeling and testing of polycrystalline hastelloy-X." *International Journal of Solids and Structures* 29, no. 21 (1992): 2623-2638.
- [6] Coakley, James, and David Dye. "Lattice strain evolution in a high volume fraction polycrystal nickel superalloy." *Scripta Materialia* 67, no. 5 (2012): 435-438.
- [7] Mannan, Sarwan K. and Brett Clark Puckett. "Physical Metallurgy of Alloys 718, 925, 725, and 725HS for Service in Aggressive Corrosion Environments." *Corrosion* (2003)
- [8] Esmaeilizadeh, Reza, Ali Keshavarzkermani, Usman Ali, Behzad Behraves, Ali Bonakdar, Hamid Jahed, and Ehsan Toyserkani. "On the effect of laser powder-bed fusion process parameters on quasi-static and fatigue behaviour of Hastelloy X: A microstructure/defect interaction study." *Additive Manufacturing* 38 (2021): 101805.

- [9] Fayazfar, Haniyeh, Mehrnaz Salarian, Allan Rogalsky, Dyuti Sarker, Paola Russo, Vlad Paserin, and Ehsan Toyserkani. "A critical review of powder-based additive manufacturing of ferrous alloys: Process parameters, microstructure and mechanical properties." *Materials & Design* 144 (2018): 98-128.
- [10] Shamsaei, Nima, Aref Yadollahi, Linkan Bian, and Scott M. Thompson. "An overview of Direct Laser Deposition for additive manufacturing; Part II: Mechanical behavior, process parameter optimization and control." *Additive Manufacturing* 8 (2015): 12-35.
- [11] Laeng, James, J. G. Stewart, and Frank W. Liou. "Laser metal forming processes for rapid prototyping-A review." *International Journal of Production Research* 38, no. 16 (2000): 3973-3996.
- [12] Bremen, Sebastian, Wilhelm Meiners, and Andrei Diatlov. "Selective laser melting: a manufacturing technology for the future?." *Laser Technik Journal* 9, no. 2 (2012): 33-38.
- [13] Sanchez-Mata, Oscar, Xianglong Wang, Jose Alberto Muniz-Lerma, Sila Ece Atabay, Mohammad Attarian Shandiz, and Mathieu Brochu. "Dependence of mechanical properties on crystallographic orientation in nickel-based superalloy Hastelloy X fabricated by laser powder bed fusion." *Journal of Alloys and Compounds* 865 (2021): 158868.
- [14] Kamath, Chandrika, Bassem El-Dasher, Gilbert F. Gallegos, Wayne E. King, and Aaron Sisto. "Density of additively-manufactured, 316L SS parts using laser powder-bed fusion at powers up to 400 W." *The International Journal of Advanced Manufacturing Technology* 74, no. 1 (2014): 65-78.
- [15] Ni, Xiaoqing, Decheng Kong, Liang Zhang, Chaofang Dong, Jia Song, and Wenheng Wu. "Effect of process parameters on the mechanical properties of hastelloy X alloy fabricated by selective laser melting." *Journal of Materials Engineering and Performance* 28, no. 9 (2019): 5533-5540.

- [16] Esmaeilizadeh, Reza, Ali Keshavarzkermani, Usman Ali, Yahya Mahmoodkhani, Behzad Behraves, Hamid Jahed, Ali Bonakdar, and Ehsan Toyserkani. "Customizing mechanical properties of additively manufactured Hastelloy X parts by adjusting laser scanning speed." *Journal of Alloys and Compounds* 812 (2020): 152097.
- [17] Bahador, Abdollah, Junko Umeda, Esah Hamzah, Farazila Yusof, Xiaochun Li, and Katsuyoshi Kondoh. "Synergistic strengthening mechanisms of copper matrix composites with TiO<sub>2</sub> nanoparticles." *Materials Science and Engineering: A* 772 (2020): 138797.
- [18] Gornet, T., and T. Wohlers. "History of additive manufacturing non-SL systems Introduction of low-cost 3D printers." Fort Collins, Co: Wohlers Associates Inc (2016): 1-38.
- [19] Hanzl, Pavel, Miroslav Zetek, Tomáš Bakša, and Tomáš Kroupa. "The influence of processing parameters on the mechanical properties of SLM parts." *Procedia Engineering* 100 (2015): 1405-1413.
- [20] Wong, K. V., and A. Hernandez. "A review of additive manufacturing. *ISRN Mech. Eng.* 2012, 1–10 (2012)."
- [21] Wang, Kaiming, Dong Du, Guan Liu, Ze Pu, Baohua Chang, and Jiang Ju. "A study on the additive manufacturing of a high chromium Nickel-based superalloy by extreme high-speed laser metal deposition." *Optics & Laser Technology* 133 (2021): 106504.
- [22] Montero-Sistiaga, Maria L., Saeid Pourbabak, Jan Van Humbeeck, Dominique Schryvers, and Kim Vanmeensel. "Microstructure and mechanical properties of Hastelloy X produced by HP-SLM (high power selective laser melting)." *Materials & Design* 165 (2019): 107598.
- [23] Tomus, Dacian, Yang Tian, Paul A. Rometsch, Martin Heilmaier, and Xinhua Wu. "Influence of post heat treatments on anisotropy of mechanical behaviour and microstructure of Hastelloy-X parts produced by selective laser melting." *Materials Science and Engineering: A* 667 (2016): 42-53.



- [24] Wang, F. W. X. H., Xin Hua Wu, and Daniel Clark. "On direct laser deposited Hastelloy X: dimension, surface finish, microstructure and mechanical properties." *Materials Science and Technology* 27, no. 1 (2011): 344-356.
- [25] Liverani, Erica, Stefania Toschi, Lorella Ceschini, and Alessandro Fortunato. "Effect of selective laser melting (SLM) process parameters on microstructure and mechanical properties of 316L austenitic stainless steel." *Journal of Materials Processing Technology* 249 (2017): 255-263.
- [26] Wang, Yachao, and Jing Shi. "Developing very strong texture in a nickel-based superalloy by selective laser melting with an ultra-high power and flat-top laser beam." *Materials Characterization* 165 (2020): 110372.
- [27] Ezugwu, E. O., J. Bonney, and Yasuo Yamane. "An overview of the machinability of aeroengine alloys." *Journal of materials processing technology* 134, no. 2 (2003): 233-253.
- [28] Zhao, Shuangqun, Xishan Xie, Gaylord D. Smith, and Shailesh J. Patel. "Microstructural stability and mechanical properties of a new nickel-based superalloy." *Materials Science and Engineering: A* 355, no. 1-2 (2003): 96-105.
- [29] Zhang, Chengjiang, Ping Wang, Zhixun Wen, Zhuangzhuang Xu, Pengfei He, and Zhufeng Yue. "Study on creep properties of nickel-based superalloy blades based on microstructure characteristics." *Journal of Alloys and Compounds* 890 (2022): 161710.
- [30] Thellaputta, Gopala Rao, Pulcharu Subhash Chandra, and C. S. P. Rao. "Machinability of nickel based superalloys: a review." *Materials Today: Proceedings* 4, no. 2 (2017): 3712-3721.
- [31] Pervaiz, Salman, Amir Rashid, Ibrahim Deiab, and Mihai Nicolescu. "Influence of tool materials on machinability of titanium-and nickel-based alloys: a review." *Materials and Manufacturing Processes* 29, no. 3 (2014): 219-252.
- [32] Lange, Fred F. "Powder processing science and technology for increased reliability." *Journal of the American Ceramic Society* 72, no. 1 (1989): 3-15.

- [33] Huang, Yong, Ming C. Leu, Jyoti Mazumder, and Alkan Donmez. "Additive manufacturing: current state, future potential, gaps and needs, and recommendations." *Journal of Manufacturing Science and Engineering* 137, no. 1 (2015).
- [34] Carter, Luke N., Christopher Martin, Philip J. Withers, and Moataz M. Attallah. "The influence of the laser scan strategy on grain structure and cracking behaviour in SLM powder-bed fabricated nickel superalloy." *Journal of Alloys and Compounds* 615 (2014): 338-347.
- [35] Babu, Sudarsanam Suresh, Narendran Raghavan, Jacob Raplee, Sarah J. Foster, Curtis Frederick, Michael Haines, R. Dinwiddie et al. "Additive manufacturing of nickel superalloys: opportunities for innovation and challenges related to qualification." *Metallurgical and Materials Transactions A* 49, no. 9 (2018): 3764-3780.
- [36] Soffel, Fabian, Yunong Lin, Dominik Keller, Sergei Egorov, and Konrad Wegener. "Laser Remelting Process Simulation and Optimization for Additive Manufacturing of Nickel-Based Super Alloys." *Materials* 15, no. 1 (2021): 177.
- [37] Graybill, Benjamin, Ming Li, David Malawey, Chao Ma, Juan-Manuel Alvarado-Orozco, and Enrique Martinez-Franco. "Additive manufacturing of nickel-based superalloys." In *International Manufacturing Science and Engineering Conference*, vol. 51357, p. V001T01A015. American Society of Mechanical Engineers, 2018.
- [38] Chatzidakis, Stylianos, Wei Tang, Roger Miller, Andrew Payzant, Jeff Bunn, Charles Bryan, John Scaglione, and Jy-An Wang. "Neutron diffraction illustrates residual stress behavior of welded alloys used as radioactive confinement boundary." *International Journal of Pressure Vessels and Piping* 191 (2021): 104348.
- [39] Hutchings, Michael T., Philip J. Withers, Thomas M. Holden, and Torben Lorentzen. "Introduction to the characterization of residual stress by neutron diffraction." CRC press, 2005.

- [40] Engler, O., and V. Randle. "Introduction to Texture Analysis Macrotexture, Microtexture and Orientation Mapping." CRC press, 2010.
- [41] Xu, Feng. Lattice strain and texture evolution during room-temperature deformation in Zircaloy-2. Queen's University, 2007.
- [42] Xu, F., R. A. Holt, M. R. Daymond, R. B. Rogge, and E. C. Oliver. "Development of internal strains in textured Zircaloy-2 during uni-axial deformation." *Materials Science and Engineering: A* 488, no. 1-2 (2008): 172-185.
- [43] Xu, F., R. A. Holt, and M. R. Daymond. "Modeling texture evolution during uni-axial deformation of Zircaloy-2." *Journal of nuclear materials* 394, no. 1 (2009): 9-19.
- [44] Grant, Benedict MB, Elisabeth M. Francis, Joao Quinta Da Fonseca, Mark R. Daymond, and Michael Preuss. "Deformation behaviour of an advanced nickel-based superalloy studied by neutron diffraction and electron microscopy." *Acta materialia* 60, no. 19 (2012): 6829-6841.
- [45] Collins, David M., Neil D'Souza, and Chinnapat Panwisawas. "In-situ neutron diffraction during stress relaxation of a single crystal nickel-base superalloy." *Scripta Materialia* 131 (2017): 103-107.
- [46] Bragg, W. L. "X-ray diffraction and crystal structure." *Proc. Roy. Soc. A* 89 (1913): 248-77.
- [47] Santisteban, J. R., M. R. Daymond, J. A. James, and L. Edwards. "ENGIN-X: a third-generation neutron strain scanner." *Journal of Applied Crystallography* 39, no. 6 (2006): 812-825.
- [48] Nishikawa, S. H. O. J. I., and S. E. I. S. H. I. Kikuchi. "Diffraction of cathode rays by calcite." *Nature* 122, no. 3080 (1928): 726-726.
- [49] Lin, Y. C., Dao-Guang He, Ming-Song Chen, Xiao-Min Chen, Chun-Yang Zhao, Xiang Ma, and Zhi-Li Long. "EBSD analysis of evolution of dynamic recrystallization grains and  $\delta$  phase in a nickel-based superalloy during hot compressive deformation." *Materials & Design* 97 (2016): 13-24.

- [50] Taylor, Geoffrey Ingram, and Constance F. Elam. "Bakerian lecture: the distortion of an aluminium crystal during a tensile test." *Proceedings of the Royal Society of London. Series A, Containing Papers of a Mathematical and Physical Character* 102, no. 719 (1923): 643-667.
- [51] Schmid, Erich, and Walter Boas. "Plasticity of crystals." , Chapman and Hill, London (1950).
- [52] Taylor, Geoffrey Ingram. "Plastic strain in metals." *J. Inst. Metals* 62 (1938): 307-324.
- [53] Eshelby, John Douglas. "The determination of the elastic field of an ellipsoidal inclusion, and related problems." *Proceedings of the royal society of London. Series A. Mathematical and physical sciences* 241, no. 1226 (1957): 376-396.
- [54] Kröner, E. "Zur plastischen verformung des vielkristalls." *Acta metallurgica* 9, no. 2 (1961): 155-161.
- [55] Rowley, M. A., and E. A. Thornton. "Constitutive modeling of the visco-plastic response of Hastelloy-X and aluminum alloy 8009." (1996): 19-27.
- [56] Lebensohn, Ricardo A. "N-site modeling of a 3D viscoplastic polycrystal using fast Fourier transform." *Acta materialia* 49, no. 14 (2001): 2723-2737.
- [57] Lee, S-B., R. A. Lebensohn, and Anthony D. Rollett. "Modeling the viscoplastic micromechanical response of two-phase materials using Fast Fourier Transforms." *International Journal of Plasticity* 27, no. 5 (2011): 707-727.
- [58] Lebensohn, Ricardo A., Anand K. Kanjarla, and Philip Eisenlohr. "An elasto-viscoplastic formulation based on fast Fourier transforms for the prediction of micromechanical fields in polycrystalline materials." *International Journal of Plasticity* 32 (2012): 59-69.
- [59] Hill, Rodney. "Generalized constitutive relations for incremental deformation of metal crystals by multislip." *Journal of the Mechanics and Physics of Solids* 14, no. 2 (1966): 95-102.

- [60] Rice, James R. "Inelastic constitutive relations for solids: an internal-variable theory and its application to metal plasticity." *Journal of the Mechanics and Physics of Solids* 19, no. 6 (1971): 433-455.
- [61] Hill, R., and JR0254 Rice. "Constitutive analysis of elastic-plastic crystals at arbitrary strain." *Journal of the Mechanics and Physics of Solids* 20, no. 6 (1972): 401-413.
- [62] Asaro, Robert J. "Crystal plasticity." *Journal of Applied Mechanics* 50 (1983): 921-934.
- [63] Peirce, D., R. J. Asaro, and A. Needleman. "An analysis of nonuniform and localized deformation in ductile single crystals." *Acta metallurgica* 30, no. 6 (1982): 1087-1119.
- [64] Asaro, Robert J., and JR0375 Rice. "Strain localization in ductile single crystals." *Journal of the Mechanics and Physics of Solids* 25, no. 5 (1977): 309-338.
- [65] Asaro, R. J., and A. Needleman. "Overview no. 42." *Texture development and strain hardening in rate dependent polycrystals. Acta Metallurgica* 33 (1985): 923-953.
- [66] Bishop, J. F. W., and Rodney Hill. "XLVI. A theory of the plastic distortion of a polycrystalline aggregate under combined stresses." *The London, Edinburgh, and Dublin Philosophical Magazine and Journal of Science* 42, no. 327 (1951): 414-427.
- [67] Toth, L. S., P. Gilormini, and J. J. Jonas. "Effect of rate sensitivity on the stability of torsion textures." *Acta Metallurgica* 36, no. 12 (1988): 3077-3091.
- [68] Wu, Tien-Yue, John L. Bassani, and Campbell Laird. "Latent hardening in single crystals-I. Theory and experiments." *Proceedings of the Royal Society of London. Series A: Mathematical and Physical Sciences* 435, no. 1893 (1991): 1-19.
- [69] Bassani, John L., and Tien-Yue Wu. "Latent hardening in single crystals. II. Analytical characterization and predictions." *Proceedings of the Royal Society of London. Series A: Mathematical and Physical Sciences* 435, no. 1893 (1991): 21-41.

- [70] Tome, C., G. R. Canova, U. F. Kocks, N. Christodoulou, and J. J. Jonas. "The relation between macroscopic and microscopic strain hardening in FCC polycrystals." *Acta metallurgica* 32, no. 10 (1984): 1637-1653.
- [71] Xu, F., R. A. Holt, and M. R. Daymond. "Modeling lattice strain evolution during uniaxial deformation of textured Zircaloy-2." *Acta Materialia* 56, no. 14 (2008): 3672-3687.
- [72] Mareau, C., and M. R. Daymond. "Study of internal strain evolution in Zircaloy-2 using polycrystalline models: Comparison between a rate-dependent and a rate-independent formulation." *Acta Materialia* 58, no. 9 (2010): 3313-3325.
- [73] Elshwain, A. E. I., Norizah Redzuan, and Noordin Mohd Yusof. "Machinability of Nickel and Titanium alloys under of gas-based coolant-lubricants (cls)—A Review." *International Journal of Research in Engineering and Technology* 2, no. 11 (2013): 690-702.
- [74] von Kobylinski, Jonas, Robert Lawitzki, Michael Hofmann, Christian Kremphaszky, and Ewald Werner. "Micromechanical behaviour of Ni-based superalloys close to the yield point: a comparative study between neutron diffraction on different polycrystalline microstructures and crystal plasticity finite element modelling." *Continuum Mechanics and Thermodynamics* 31, no. 3 (2019): 691-702.
- [75] Abuzaid, Wael Z., Michael D. Sangid, Jay D. Carroll, Huseyin Sehitoglu, and John Lambros. "Slip transfer and plastic strain accumulation across grain boundaries in Hastelloy X." *Journal of the Mechanics and Physics of Solids* 60, no. 6 (2012): 1201-1220.
- [76] Dang, C. X., P. Zhang, J. Li, Z. H. Gao, B. Li, X. F. Gong, and X. L. Song. "The role of  $\langle 112 \rangle\{111\}$  slip in the initial plastic deformation of Ni-base superalloys at room temperature." *Materials Characterization* 170 (2020): 110648.
- [77] Abuzaid, W., and L. Patriarca. "A study on slip activation for a coarse-grained and single crystalline CoCrNi medium entropy alloy." *Intermetallics* 117 (2020): 106682.

- [78] Xu, Feng. Lattice strain and texture evolution during room-temperature deformation in Zircaloy-2. Queen's University, 2007.
- [79] Cheng, Jiahao, and Somnath Ghosh. "Crystal plasticity finite element modeling of discrete twin evolution in polycrystalline magnesium." *Journal of the Mechanics and Physics of Solids* 99 (2017): 512-538.
- [80] Geng, Yaoyi, and Noel Harrison. "Functionally graded bimodal Ti6Al4V fabricated by powder bed fusion additive manufacturing: Crystal plasticity finite element modelling." *Materials Science and Engineering: A* 773 (2020): 138736.
- [81] Abdolvand, Hamidreza, Mark R. Daymond, and Charles Mareau. "Incorporation of twinning into a crystal plasticity finite element model: Evolution of lattice strains and texture in Zircaloy-2." *International Journal of Plasticity* 27, no. 11 (2011): 1721-1738.
- [82] Zhang, Dongxu, Jinyang He, Jianwei Liang, and Zhou He. "Surface Slip Deformation Characteristics of Nickel-Base Single Crystal Thin Plates With Film Cooling Holes." *IEEE Access* 8 (2020): 75145-75153.
- [83] Yuan, Guang-Jian, Xian-Cheng Zhang, Bo Chen, Shan-Tung Tu, and Cheng-Cheng Zhang. "Low-cycle fatigue life prediction of a polycrystalline nickel-base superalloy using crystal plasticity modelling approach." *Journal of Materials Science & Technology* 38 (2020): 28-38.
- [84] Moghaddam, Masoud Ghorbani, Ajit Achuthan, Brett A. Bednarczyk, Steven M. Arnold, and Evan J. Pineda. "Grain size-dependent crystal plasticity constitutive model for polycrystal materials." *Materials Science and Engineering: A* 703 (2017): 521-532.
- [85] Fischer, Tim, Ewald Werner, and Oliver Munz. "Crystal plasticity modeling of polycrystalline Ni-base superalloy honeycombs under combined thermo-mechanical loading." *Continuum Mechanics and Thermodynamics* 31, no. 3 (2019): 703-713.

- [86] Wei, H. L., J. Mazumder, and Tarasankar DebRoy. "Evolution of solidification texture during additive manufacturing." *Scientific reports* 5, no. 1 (2015): 1-7.
- [87] Pham, Minh-Son, Bogdan Dovggy, Paul A. Hooper, Christopher M. Gurlay, and Alessandro Piglione. "The role of side-branching in microstructure development in laser powder-bed fusion." *Nature communications* 11, no. 1 (2020): 1-12.
- [88] Pauza, J. G., W. A. Tayon, and A. D. Rollett. "Computer simulation of microstructure development in powder-bed additive manufacturing with crystallographic texture." *Modelling and Simulation in Materials Science and Engineering* 29, no. 5 (2021): 055019.



## Figures' Permission

- Figure. 2-2 The main process parameters for the laser power bed technique [9]

---

**From:** Permissions Helpdesk

**Sent:** June 14, 2022 9:23 AM

**To:** Ahmed Aburakhia

**Subject:** Re: Requesting Permission [220614-000950]

Dear Ahmed Aburakhia, Thank you

for your email.

We hereby grant you permission to reprint the material below at no charge in your thesis subject to the following conditions:

1. If any part of the material to be used (for example, figures) has appeared in our publication with credit or acknowledgement to another source, permission must also be sought from that source. If such permission is not obtained then that material may not be included in your publication/copies.

2. Suitable acknowledgment to the source must be made, either as a footnote or in a reference list at the end of your publication, as follows:

"This article was published in Publication title, Vol number, Author(s), Title of article, Page Nos, Copyright Elsevier (or appropriate Society name) (Year)."

3. Your thesis may be submitted to your institution in either print or electronic form.

4. Reproduction of this material is confined to the purpose for which permission is hereby given

5. This permission is granted for non-exclusive world English rights only. For other languages please reapply separately for each one required. Permission excludes use in an electronic form other than submission. Should you have a

specific electronic project in mind please reapply for permission.

6. Should your thesis be published commercially, please reapply for permission.

This includes permission for the Library and Archives of Canada to supply single copies, on demand, of the complete thesis. Should your thesis be published commercially, please reapply for

permission- Canada

This includes permission for UMI to supply single copies, on demand, of the complete thesis. Should your thesis be published commercially, please reapply for permission-ROW

7. Posting of the full article online is not permitted. You may post an abstract with a link to the Elsevier website [www.elsevier.com](http://www.elsevier.com), or to the article on ScienceDirect if it is available on that platform.

8. Article can used be in the University library if it is embedded in the thesis and not used commercially.

Kind regards,

**Thomas Rexson Yesudoss**

Copyrights Coordinator

ELSEVIER | HCM - Health Content Management Visit [Elsevier.Permissions](http://Elsevier.Permissions)

- Figure. 2-3 a, b: Fracture surface of a sample manufactured using non-optimum process conditions, arrows point to unmelted powder particles; c, d fracture surface of the sample that was manufactured using optimum process conditions [24]

---

**From:** Journal Permissions

**Sent:** June 14, 2022 5:03 AM

**To:** Ahmed Aburakhia

**Subject:** RE: ymst20:On direct laser deposited Hastelloy X: dimension, surface finish, microstructure and mechanical properties

Good Morning,

Thank you for your correspondence requesting permission to reproduce content from a Taylor & Francis Group content from our Journal in your thesis to be posted on your University's repository.

We will be pleased to grant the permission without fee on the condition that you acknowledge the original source of publication and insert a reference to the Journal's web site: [www.tandfonline.com](http://www.tandfonline.com)

**This permission does not cover any third party copyrighted work which may appear in the material requested. Please ensure you have checked all original source details for the rights holder.**

Please note that this licence **does not allow you to post our content on any third-party websites.**

Thank you for your interest in our Journal. With best wishes,

**Journals Permissions Team,**

Journals, Taylor & Francis Group

**Permissions e-mail:** [JournalPermissions@tandf.co.uk](mailto:JournalPermissions@tandf.co.uk) **Web:** [www.tandfonline.com](http://www.tandfonline.com)

@ 4 Park Square, Milton Park, Abingdon, OX14 4RN

if **+44 (0)20 8052 0600**



Taylor & Francis is a trading name of Informa UK Limited, registered in England under no. 1072954

- Figure. 2-5 (a) Schematic of ENGIN-X Neutron Diffractometer [47]



**Terms and conditions of use of the article titled**

**ENGIN-X: a third-generation neutron strain scanner**

[Santisteban *et al.* (2006). *J. Appl. Cryst.* **39**; 812-825

<https://doi.org/10.1107/S0021889806042245>]

Permission to reproduce or reuse in whole or part the above article is granted to

Anmed Aouraknia

Provided that the reused material is accompanied by an attribution statement according to the terms of the open-access licence under which the original article was published, and that permission has been obtained **from** any other organizations or individuals where any parts of the material are subject to explicit statements of copyright or prior reproduction permission from such third parties.



Peter Shickfand

Executive Managing Editor, IUCr Journals

- Figure. 2-6 Schematic representation of Voce hardening law.  $\theta_0$  and  $\theta_1$  are the voce hardening parameters. [70]

---

**From:** Permissions Helpdesk

**Sent:** June 14, 2022 9:25 AM

**To:** Ahmed Aburakhia

**Subject:** Re: Requesting Permission [220614-002744]

Dear Ahmed Aburakhia, Thank

you for your email.

We hereby grant you permission to reprint the material below at no charge in your thesis subject to the following conditions:

1. If any part of the material to be used (for example, figures) has appeared in our publication with credit or acknowledgement to another source, permission must also be sought from that source. If such permission is not obtained then that material may not be included in your publication/copies.

2. Suitable acknowledgment to the source must be made, either as a footnote or in a reference list at the end of your publication, as follows:

"This article was published in Publication title, Vol number, Author(s), Title of article, Page Nos, Copyright Elsevier (or appropriate Society name) (Year)."

3. Your thesis may be submitted to your institution in either print or electronic form.

4. Reproduction of this material is confined to the purpose for which permission is hereby given

5. This permission is granted for non-exclusive world English rights only. For other languages please reapply separately for each one required. Permission excludes use in an electronic form other than submission. Should you have a

specific electronic project in mind please reapply for permission.

6. Should your thesis be published commercially, please reapply for permission.

This includes permission for the Library and Archives of Canada to supply single copies, on demand, of the complete thesis. Should your thesis be published commercially, please reapply for permission- Canada

This includes permission for UMI to supply single copies, on demand, of the complete thesis. Should your thesis be published commercially, please reapply for permission-ROW

7. Posting of the full article online is not permitted. You may post an abstract with a link to the Elsevier website [www.elsevier.com](http://www.elsevier.com), or to the article on ScienceDirect if it is available on that platform.

8. Article can used be in the University library if it is embedded in the thesis and not used commercially.

Kind regards,

**Thomas Rexson Yesudoss**

Copyrights Coordinator

ELSEVIER | HCM - Health Content Management Visit [Elsevier](http://Elsevier)

[Permissions](#)

## Curriculum Vitae

<b>Name:</b>	Ahmed Aburakhia
<b>Post-secondary Education and Degrees:</b>	King Fahd University of Petroleum and Minerals Dhahran, Saudi Arabia 2012-2016 Master of Engineering Managment
	King Fahd University of Petroleum and Minerals Dhahran, Saudi Arabia 2008-2012 B.Sc. Mechanical Engineering
<b>Honours and Awards:</b>	Western Graduate Research Scholarship 2020-2022
	First Honor Degree in B.Sc. Mechanical Engineering 2008-2012
<b>Related Work Experience</b>	Teaching Assistant / Research Assistant The University of Western Ontario 2020-2022
	Senior Technical Professional Halliburton Energy Services, 2019-2020
	Technical Sales Representative Weatherford Energy Services, 2013-2019